

# Ambient Seismic Recordings and Distributed Acoustic Sensing (DAS): Imaging the firn layer on Rutford Ice Stream, Antarctica

Wen Zhou<sup>1,1</sup>, Antony Butcher<sup>1,1</sup>, Alex Mark Brisbane<sup>2,2</sup>, Sofia-Katerina Kufner<sup>2,2</sup>, John-Michael Kendall<sup>3,3</sup>, and Anna Stork<sup>4,4</sup>

<sup>1</sup>University of Bristol

<sup>2</sup>British Antarctic Survey

<sup>3</sup>University of Oxford

<sup>4</sup>Silixa

November 30, 2022

## Abstract

Distributed acoustic sensing (DAS) is a rapidly growing seismic technology, which provides near-continuous spatial sampling, low maintenance, long-term deployments, can exploit extensive cable networks already deployed in many environments. Here, we present a case study from the Rutford Ice Stream, Antarctica, showing how the ice-sheet firn layer can be imaged with DAS and seismic interferometry, exploiting noise from a power generator and fracturing at the ice stream margin. Conventional cross-correlation interferometry between DAS channels yields an unstable seismic response. Instead, we present two strategies to improve interferograms: (1) combining signals from conventional seismic instruments with DAS; (2) selective-stacking cross-correlation. These steps yield high-quality Rayleigh wave responses. We validate our approach with a dataset acquired using a sledgehammer-and-plate source, and show an excellent agreement between the dispersion curves. The passive results display a lower frequency content ( $\sim 3$ Hz) than the active datasets ( $\sim 10$ Hz). A 1D S-wave velocity profile is inverted for the top 100m of the glacier, which contains inflections as predicted by firn densification models. Using a triangular DAS array, we repeat the noise interferometry analysis and find no visible effect of seismic anisotropy in the uppermost 80 meters of our study site. Results presented here highlight the potential of DAS and surface wave inversions to complement conventional refraction surveys, which are often used for imaging firn layer, and the potential in near-surface imaging applications in general.

1 **Seismic noise interferometry and Distributed Acoustic Sensing (DAS): measuring the**  
2 **firn layer S-velocity structure on Rutford Ice Stream, Antarctica**

3 **Wen Zhou<sup>1</sup>, Antony Butcher<sup>1</sup>, Alex Brisbourne<sup>2</sup>, Sofia-Katerina Kufner<sup>2</sup>, J-Michael**  
4 **Kendall<sup>3</sup>, Anna Stork<sup>4</sup>**

5 <sup>1</sup>University of Bristol, BS8 1TH, Bristol, UK

6 <sup>2</sup>British Antarctic Survey, CB3 0ET, Cambridge, UK

7 <sup>3</sup>University of Oxford, OX1 2JD, Oxford, UK

8 <sup>4</sup>Silixa, WD6 3SN, Borehamwood, UK

9 Corresponding author: Wen Zhou (wz18709@bristol.ac.uk)

10 **Key Points:**

- 11 • DAS is used for the first time to image the S-wave velocity structure and anisotropy of  
12 the firn layer in Antarctica.
- 13 • DAS seismic interferograms are greatly improved through selective stacking and cross-  
14 correlation with a geophone.
- 15 • Our method is suitable for large-scale measurements and is feasible in the presence of  
16 ice lenses where refraction methods are inadequate.
- 17
- 18

19 **Abstract**

20 Firn densification profiles are an important parameter for ice-sheet mass balance and  
21 palaeoclimate studies. One conventional method of investigating firn profiles is using seismic  
22 refraction surveys, but these are limited to point measurements. Distributed acoustic sensing  
23 (DAS) presents an opportunity for large-scale seismic measurements of firn with dense spatial  
24 sampling and easy deployment, especially when seismic noise is used. We study the feasibility of  
25 seismic noise interferometry on DAS data for characterizing the firn layer at the Rutford Ice  
26 Stream, West Antarctica. Dominant seismic energy appears to come from anthropogenic noise  
27 and shear-margin crevasses. The DAS cross-correlation interferometry yields a noisy Green's  
28 function (Rayleigh waves). To overcome this, we present two strategies for cross-correlations:  
29 (1) hybrid instruments – correlating a geophone with DAS, and (2) selected stacking where the  
30 cross-correlation panels are picked in the tau-p domain. These approaches are validated with  
31 results derived from an active survey. Using the retrieved Rayleigh wave dispersion curve, we  
32 inverted for a high-resolution 1D S-wave velocity profile down to a depth of 100 m. The  
33 inversion spontaneously retrieves a 'kink' (velocity gradient inflection) at ~12 m depth, resulting  
34 from a change of compaction mechanism. A triangular DAS array is used to investigate  
35 directional variation in velocity, which shows no evident variations thus suggesting a lack of  
36 deformation in the firn. Our results demonstrate the potential of using DAS and seismic noise  
37 interferometry to image the near-surface and present a new approach to derive S-velocity profiles  
38 from surface wave inversion in firn studies.

39 **Plain Language Summary**

40 The density distribution (density versus depth) of tens of meters at the top of a glacier is an  
41 important feature of ice-sheet mass balance and palaeoclimate research. It can be estimated using

42 the empirical relationship between density and seismic P-wave velocity. The P-wave velocity  
43 can be measured using a seismic refraction survey with geophones and active sources. However,  
44 refraction seismic surveys are expensive for measurements over large areas. Distributed Acoustic  
45 Sensing (DAS) using fibre optic cables to detect seismic waves is an emerging dense spatial  
46 sampling seismic acquisition technology. It can be used in conjunction with seismic noise cross-  
47 correlation to make large-scale measurements easier and cheaper than with conventional  
48 geophones. We investigate the feasibility of this approach on Rutford Ice Stream, West  
49 Antarctica, and propose two approaches to improve DAS seismic-noise cross-correlation results.  
50 Surface waves are retrieved by seismic noise cross-correlation and are used to estimate the S-  
51 wave velocity structure. Our S-velocity profile resembles an independently measured P-velocity  
52 in-shape and spontaneously retrieved a velocity gradient inflection—related to changes in the ice  
53 compaction mechanism. We show that DAS and seismic noise interferometry can be used for  
54 future firn measurements, but also more generally in studies of the near-surface.

## 55 **1 Introduction**

56 Firn is partially compacted granular snow, the intermediate stage between fresh snow and the  
57 underlying glacial ice. It has a depth-increasing density resulting from burial by subsequent  
58 accumulation the overburdened weight compacts the snow and reduces porosity by grain  
59 packing, deformation, and sintering (Alley, 1987; Cuffey & Paterson, 2010). The depth-density  
60 profile is controlled primarily by the temperature and snow accumulation rate and is highly  
61 variable due to the broad range of climatic conditions across the Antarctica continent (e.g., van  
62 den Broeke, 2008). Knowledge of the firn layer is crucial for improving altimetric mass-balance  
63 estimates (Shepherd et al., 2012) and palaeoclimate reconstructions (Craig et al., 1988).  
64 Additionally, studying the firn layer properties may help to constrain models of surface melt

65 leading to ice shelf retreat (van den Broeke, 2005). However, such as shear deformation along  
66 ice stream shear-margin (Riverman et al. 2019) and glacier dynamics (Hollmann et al., 2021)  
67 also influence firn structures, which suggests a comprehensive study of the Antarctica firn may  
68 be required to improve ice-sheet mass balance estimates.

69         Conventionally, the structure and densification profile of firn is directly measured from  
70 ice core or borehole logging (e.g. Morris et al., 2017), or indirectly using for example seismic P-  
71 wave refraction (e.g. Kirchner & Bentley, 1979) or radar measurements (e.g., Case & Kingslake,  
72 2022). A specific version of seismic refraction inversion was developed for the investigation of  
73 firn structures by Kirchner & Bentley (1979). The method uses curve fitting with a double-  
74 exponential form applied to diving wave travel times, prior to a Wiechert-Herglotz-Bateman  
75 (WHB) velocity-depth inversion (Slichter, 1932). These results are commonly used to correct  
76 seismic reflection surveys for near-surface effects (e.g., Peters et al., 2006; Smith, 1997), derive  
77 elastic properties of firn (King & Jarvis, 2007; Schlegel et al., 2019), and investigate its spatial  
78 variations and azimuthal anisotropy.

79         The presence of anisotropy in the firn layer has been reported previously. Kirchner &  
80 Bentley (1990) indicate substantial azimuthal anisotropy in the upper 30-40 m and state that  
81 simple transverse isotropy with a vertical symmetry axis (VTI) expected from firn compaction is  
82 not always appropriate. A recent study by Hollman et al. (2021) infers seismic anisotropy in the  
83 firn on the Amery Ice Shelf in the proximity of former shear margins. Polarimetric radar  
84 measurements have also indicated the presence of complex near-surface anisotropy on both  
85 Whillans and Rutford Ice Streams (Jordan et al, 2020; Jordan et al., 2022), in general related to  
86 ice flow and surface strain rates.

87           Although the WHB method is viable for both P- and S-wave velocity measurement, the  
88 former is by far the most widely used due to the greater ease of generation and identification of  
89 P-wave energy. However, King & Jarvis (2017) observed a variation of Poisson ratio with depth  
90 in the firn layer, suggesting that measuring S-wave velocity is important for studying firn  
91 elasticity and densification.

92           In addition, because a commonly used WHB refraction inversion method fits a double  
93 exponential velocity profile to the travel-time data, it can only apply to a typical compacted firn  
94 with monotonically increasing seismic velocity over depth and with one ‘kink’ (critical density)  
95 from a change of compaction mechanism and without any ice lenses (Kirchner & Bentley, 1979).

96           Furthermore, with conventional geophone sensors, it is time-consuming and more  
97 expensive to apply the refraction survey to cover a large area, because of the dense receiver  
98 spacing at the near offset required by the WHB inversion. Thus, most previous refraction surveys  
99 are limited to effectively -point measurements with a scale of a few hundred meters (Hollmann et  
100 al., 2021; King & Jarvis, 2007; Schlegel et al., 2019). Recently, Riverman et al (2019) conducted  
101 a 40 km refraction survey but with a sparse geophone spacing of 20 m which showed a poor  
102 resolution in the upper ~20 m of the firn.

103           Therefore, any new seismic technique capable of measuring S-wave velocities, measuring  
104 firn layer anomalies including ice lenses or low-velocity zones, or with better scaling  
105 capabilities, would be beneficial for future studies of firn. In this study, we investigate the  
106 feasibility of using DAS data, seismic noise interferometry, and surface (Rayleigh) wave  
107 inversion to address the aforementioned problem by performing distributed acoustic sensing  
108 (DAS) measurements on Rutford Ice Stream, West Antarctica.

109           In recent years, there has been a rapid development of DAS in seismic acquisition. DAS  
110 is an optical fibre sensing technology that offers the potential of broadband frequency recording  
111 and near-continuous spatial sampling of earth strain and temperature variation signals (Ajo-  
112 Franklin et al., 2019; Ide et al., 2021). Its unprecedented spatial sampling could improve the  
113 spatial resolution of subsurface seismic images (Ajo-Franklin et al., 2019; Dou et al., 2017;  
114 Lellouch et al., 2019; Rodríguez Tribaldos et al., 2019; Rodríguez Tribaldos & Ajo-Franklin,  
115 2021; Spica, Nishida, et al., 2020; Williams et al., 2019). The sensing element of DAS is the  
116 optical fibre without electronic or mechanical components, which makes the technology an  
117 attractive option for long-term, low-maintenance deployments for glacial studies (Booth et al.,  
118 2020; Brisbourne et al., 2021; Hudson et al., 2021; Walter et al., 2020), for in-situ measurement  
119 in deep boreholes for active fault (Lellouch et al., 2019), geothermal, hydrocarbon storage  
120 (Correa et al., 2018; Mateeva et al., 2017) or hydrogen storage monitoring, and for submarine  
121 environments (Lior, Sladen, et al., 2021; Spica, Nishida, et al., 2020; Williams et al., 2019). It  
122 could also be suitable for critical infrastructure (e.g. nuclear plants; Butcher et al. (2021), dams,  
123 embankments, etc).

124           Seismic noise interferometry is a simple and convenient method, from both data  
125 processing and acquisition perspectives. Many studies have used the method to retrieve surface  
126 waves for studying ice-sheets. For example, using broadband seismometers, Walter et al. (2015)  
127 used surface wave energy from crevasse events to derive the Rayleigh wave response between  
128 stations. Sergeant et al. (2020) retrieved Rayleigh waves between stations at a number of sites in  
129 Greenland and the Alps using a range of noise sources. Also, in the Alps at Glacier de la Plaine  
130 Morte, Switzerland, measurements of azimuthal variation in Rayleigh wave velocity indicate that  
131 crevasses cause up to 8% anisotropy (Lindner et al., 2019). Chaput et al. (2022) investigated

132 noise interferometry and H/V for characterising the firn layer in West Antarctica. DAS has  
133 recently been used in glacier settings for noise interferometry by Walter et al. (2020), who  
134 retrieved Rayleigh wave (above 10 Hz) from cross-correlations. However, to the best of our  
135 knowledge, no study has provided a complete S velocity profile for the glacier firn layer, which  
136 is potentially an important constraint for firn densification models.

137         It can be challenging to apply noise interferometry on DAS, especially in low ambient  
138 noise environments. Compared with conventional seismometers or geophones, DAS has higher  
139 instrument self-noise (e.g., optical system noise) which can obscure the weak seismic ‘noise’ that  
140 is the crucial ‘signal’ for noise interferometry. Nevertheless, in recent years, there have been  
141 successful applications of DAS for ambient surface wave imaging in submarine environments,  
142 using microseism noise at 0.6 – 1 Hz (Spica, Nishida, et al., 2020), 0.5 – 5 Hz (Cheng et al.,  
143 2021) and 1 – 3 Hz (Lior, Mercerat, et al., 2021). The advantage of recording in the offshore  
144 environment is the stable seafloor temperature and shorter distance to microseism noise sources.  
145 Onshore applications have been also successful (e.g., Dou et al., 2017; Rodríguez Tribaldos &  
146 Ajo-Franklin, 2021; Spica, Pertou, et al., 2020), with reported applications mostly limited to  
147 urban environments with strong anthropogenic (traffic, mechanical) noises at frequencies  
148 typically above 5 Hz. However, it is still rare to apply DAS noise interferometry in remote non-  
149 urban areas onshore.

150         In this manuscript, firstly, we present examples of raw DAS continuous recordings,  
151 which are primarily dominated by anthropogenic noise (from a snowmobile and a petro-  
152 generator) and crevasse surface wave events. We also investigate the nature of the low-frequency  
153 (< 1 Hz) part of the recording. Secondly, we demonstrate that Rayleigh waves can be retrieved  
154 through noise interferometry using data acquired on a linear DAS cable. The interferograms can

155 be improved with hybrid-instrumenting and selective stacking of noise cross-correlations.  
156 Thirdly, the fundamental mode Rayleigh wave dispersion curve is extracted and inverted to  
157 obtain an S-wave velocity ( $V_s$ ) profile. As a verification, we compare these results with  
158 dispersion analysis of the surface waves captured by an active survey using a sledgehammer and  
159 plate source. Finally, we use the data from a triangular DAS array to investigate the seismic  
160 anisotropy of the firn.

## 161 **2 Field experiment and data acquisition**

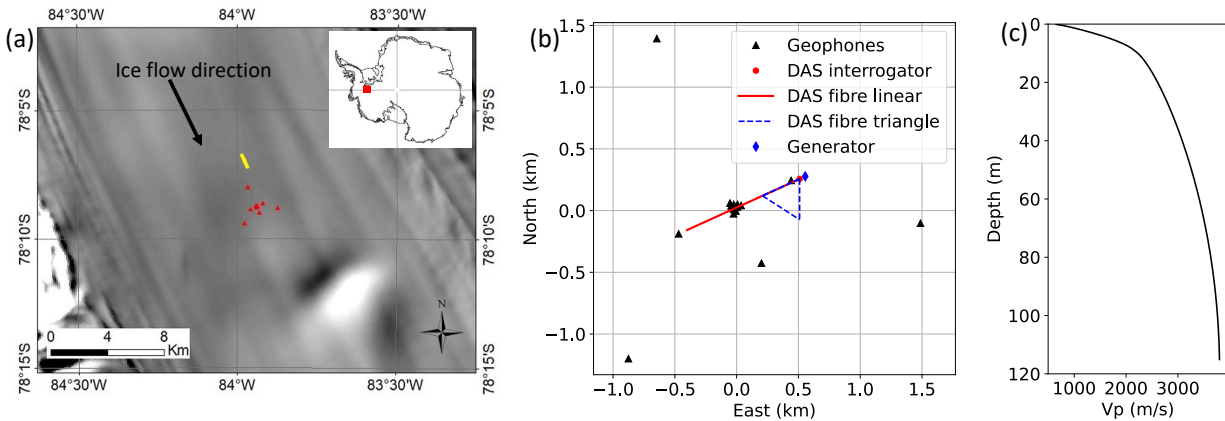
162 Rutford Ice Stream (Figure 1a) is a fast-flowing ice stream draining part of the West  
163 Antarctic Ice Sheet into the Ronne Ice Shelf. At the experiment location, 40 km upstream of the  
164 grounding line, it is around 25 km wide and 2200 m thick, with ice flow of  $\sim 380 \text{ m a}^{-1}$  (Murray  
165 et al., 2007).

166 Between 11th and 24th January 2020, an experiment was carried out at Rutford Ice  
167 Stream (Figure 1a) utilizing both DAS and geophones for passive and active surveys. The  
168 seismic arrays were collocated and installed at the centre of the ice stream where the surface is  
169 mostly flat (Figure 1a), to record the regularly occurring icequakes originating from the base of  
170 the glacier where it slides over the bed (Hudson et al., 2021; Kufner et al., 2021; Smith et al.,  
171 2015). A second aim was to image the firn layer using seismic noise and active sources. The  
172 DAS data were acquired using a Silixa iDAS v2 interrogator connected to a 1 km six channel  
173 tight buffered single mode fibre optic cable. The cable was deployed in linear and triangular  
174 configurations, successively. The iDAS measures strain rate of the optical fibre. For the passive  
175 measurement, we used a 1 kHz sampling rate, 10 m gauge length, and 1 m channel spacing. A  
176 petrol generator (Honda EU10i 1kW) was deployed as the power supply, which was located on

177 the snow surface, 50 m away from the interrogator in a direction aligned with the orientation of  
178 the fibre (Figure 1b).

179         The cable was laid in the track of a snowmobile and initially deployed without burial, but  
180 subsequently buried with a layer of approximately 5 cm of snow. Hudson et al. (2021) described  
181 these data and investigated the suitability of DAS for micro-seismicity (icequakes) monitoring.  
182 Butcher, Hudson, et al. (2021) further explored the utility of DAS data using array-based  
183 processing methods. Hudson et al. (2021) also investigated the difference between buried and  
184 unburied cable. They showed that even a shallow burial of the cable made a significant  
185 difference in attenuating the unwanted noise and enhancing the lower frequency (below 1 Hz)  
186 signal. They suggested that the better coupling to the ice results in an improved sensitivity to the  
187 primary and secondary microseisms, making it useful for ambient noise tomography studies. For  
188 frequencies 1 to 70 Hz, the buried cable has a lower noise level, thanks to its better coupling and  
189 lower wind noise. Since only the seismic noise is useful for imaging the subsurface, we  
190 concentrate on the period of time when the cable was buried.

191         The geophone network consisted of sixteen 4.5 Hz 3-component Geospace GS-11D  
192 geophones with Reftek RT130 dataloggers with a 1 kHz sample rate. The geophone array layout  
193 was primarily designed to detect and locate icequakes (Figure 1b). Three geophones were  
194 collocated or were in-line with the fibre, and they were approximately positioned in the middle  
195 and at either end of the linear DAS array.



196

197 *Figure 1. (a) Location of seismic experiment on Rutford Ice Stream. Geophone stations are shown as red dots. The background is*  
 198 *Moderate-resolution Imaging Spectroradiometer (MODIS) imagery (Scambos et al., 2007). Geophones are shown as red dots.*  
 199 *The yellow line indicates the location of a previous refraction survey (Smith et al., 2021). (b) The relative position (reference at*  
 200 *the centre of the geophone array) of instruments. Geophones (black triangles) were designed for array processing. DAS fibres*  
 201 *(red solid line and blue dashed line) were connected to the DAS interrogator at the east end. The generator (diamond) sits 50 m*  
 202 *away from the interrogator. (c) Firn P wave velocity profile from a refraction experiment (Smith et al., 2021), using an expanding*  
 203 *interval of vertical component geophones*

204

205

206

207

208

209

210

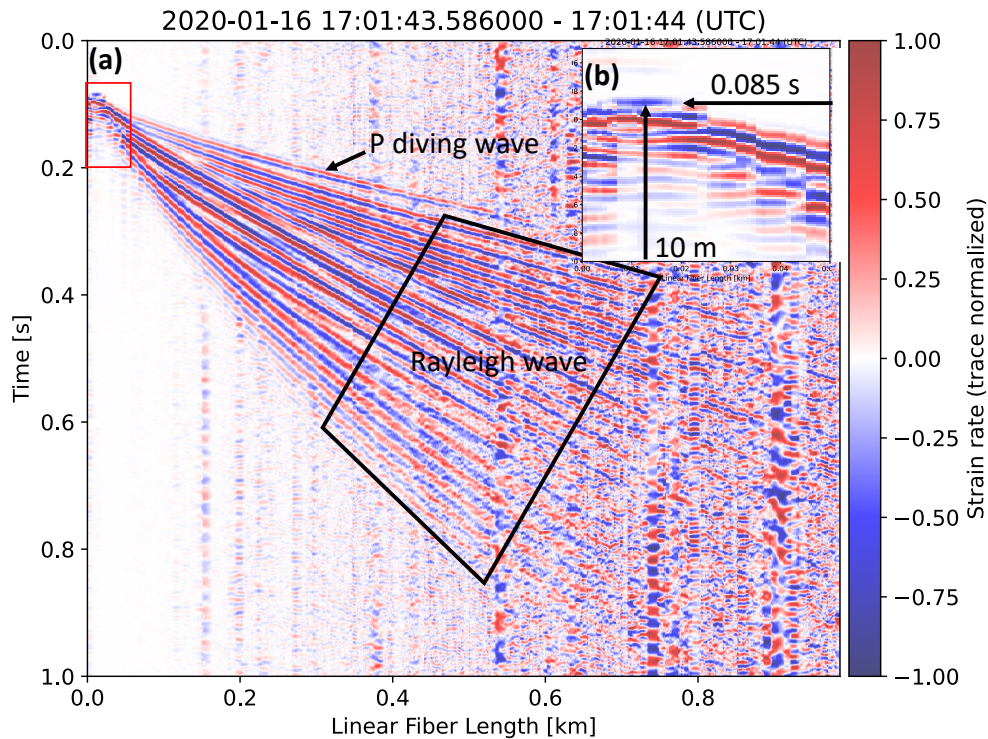
211

212

213

In addition to the passive measurements, an active seismic survey was also acquired along the linear array using a sledgehammer (4.5 kg) and plate source. These shots were recorded by the iDAS interrogator at 8 kHz sampling rate. At the 21 source locations (every 50 m from 10 to 1000m along the fibre), a total of 42 shot-gathers were acquired, with two or four shots per location. In general, the data quality of these shot-gathers is high, with signals captured across the entire 1km linear array without the need for stacking. An example shot-gather from this survey is presented in Figure 2, which shows dominant seismic phases including refracted (diving) P-waves and Rayleigh waves, as indicated. The shot times are constrained from the onset of the DAS record (Figure 2b, the first record is the strain generated by the hammer plate impact). Due to the averaging effect of the 10 m gauge length, very near offset DAS recordings

214 are distorted (Figure 2 b) which limits the accuracy of the near-surface  $V_p$  in a WHB refraction  
 215 inversion. Research on overcoming this plateau effect is working in progress.



216  
 217 *Figure 2. An example of active shot data from a hammer and plate source. (a) A shot gather on the 1 km linear fibre (1 m*  
 218 *channel distance plotted), with the source at 10 m from one end of the fibre. The strain rate waveforms are normalized over*  
 219 *each DAS channel. Signal is bandpass filtered 5 to 100 Hz. Note 0 s is not the trigger time, but an arbitrary stamp as shown in*  
 220 *the figure. (b) is a zoom-in of the (a) as indicated by the red box. Around the shot location (10 m), the first arrivals are flat, which*  
 221 *is an artefact of the 10 m gauge DAS length.*

222 A conventional P-wave seismic refraction survey was previously acquired 2.6 km  
 223 upstream of the study area (Figure 1a), using a surface source and expanding spread of vertical  
 224 component geophones out to a maximum offset of 980 m, as part of the site survey for the  
 225 BEAMISH subglacial drilling project (Smith et al., 2021). Using this refraction dataset, we  
 226 derived a P-wave velocity depth profile using the WHB based inversion method of Kirchner &  
 227 Bentley (1979) (Figure 1c). With this method, Kirchner & Bentley (1990) report velocity

228 uncertainty of  $\pm 60$  m/s near the surface, reducing to  $\pm 15$  m/s at 50 m depth on Ross Ice Shelf,  
229 which we assume similar in our inversion given the similarity of firn structures of the two sites.

### 230 **3 DAS noise characterization on the linear array**

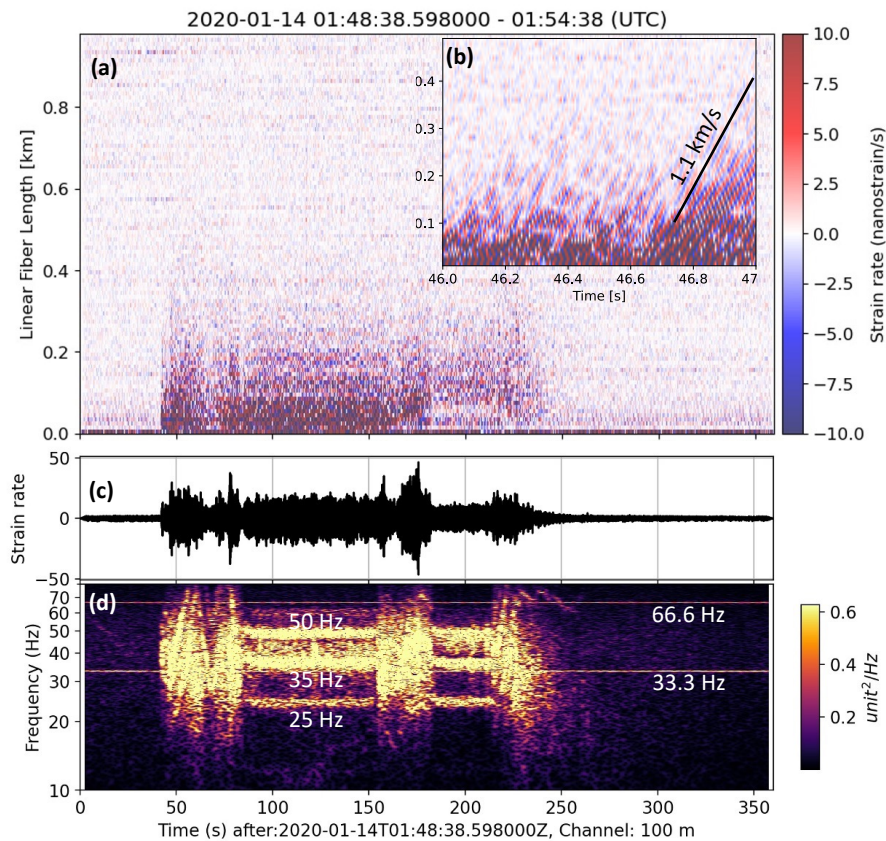
231 Prior to the noise interferometry analysis, we seek to characterise the seismic noise  
232 recorded on the DAS array, as noise interferometry is a relatively new application to DAS data in  
233 a glacial setting (Walter et al., 2020).

234 For a conventional seismic array, seismic noise is analysed with beamforming, which  
235 estimates the apparent velocity and azimuth of the coherent wavefield, such as in Chaput et al.  
236 (2022). van den Ende & Ampuero (2021) firstly applied beamforming to DAS recorded  
237 earthquake signal using a fibre with a 2D deployment. However, performing the beamforming  
238 with a 1D array results in a symmetric ambiguity. We thus simply visualize the DAS data in the  
239 time-space (time dimension in one axial direction and channel distance in the other) plot for 4  
240 frequency bands ( $< 1$  Hz, 1 – 10 Hz, and 10 -100 Hz). We then manually inspect the signal  
241 coherency. To improve the efficiency of this visualization process, we down sample the DAS  
242 channel distance to 10 m, and a sample rate of 200 Hz.

#### 243 3.1 Anthropogenic noise ( $> 10$ Hz)

244 In Figure 3 we present an example of high-frequency noise (1 Hz high-pass filtered), which  
245 began abruptly at around 45 seconds and lasted to approximately 200 seconds. It was recorded  
246 on the linear array DAS, with decreasing amplitude from 0 to  $\sim 400$  m along the cable (Figure  
247 3a). We examine the frequency content of this signal by creating a spectrogram (Figure 3c) for  
248 the record at 100 m (Figure 3b), using a short-time Fourier transform. In this record, the signal  
249 starts with a varying frequency over 10 to 70 Hz from around 45 s, then settles at a constant  
250 frequency around 25 Hz, 35 Hz and 50 Hz at  $\sim 70$  s. This vibration pattern repeats one more time,

251 before the signal gradually disappears around 250 s. We speculate that this signal is from a  
 252 snowmobile when we use it to approach the generator for refueling. The generator creates a  
 253 constant 33.3 and 66.6 Hz signal. The generator was 50 m away from the DAS channel at 0 m,  
 254 the site of the recording interrogator in a tent (Figure 1b).

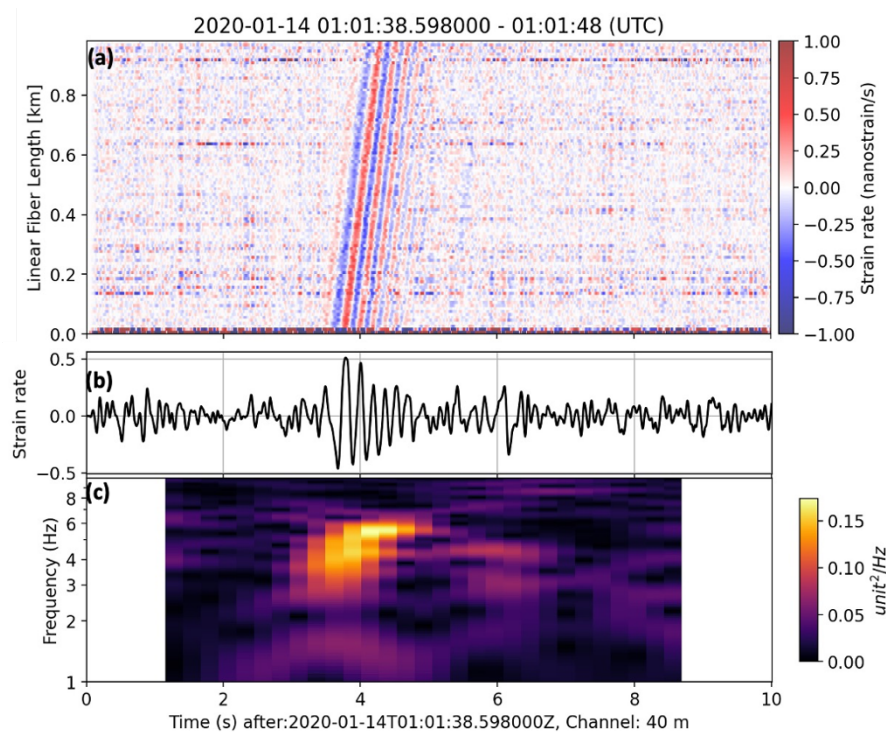


255  
 256 *Figure 3. An example of recorded anthropogenic noise. (a) Six minutes of DAS recording after median value been subtracted for*  
 257 *each time step, and bandpass filter 1 to 100 Hz, with amplitude represented in colour saturated between -10 and 10*  
 258 *nanostrain/s. (b) A zoom-in of (a) for 46-47 seconds at 0 to 500 m. (c) Time series for DAS channel at 100 m. (d) spectrogram of*  
 259 *channel 100 m calculated from FFT with a 2-second sliding window.*

### 260 3.2 Crevasse signals (1 - 10 Hz)

261 In the frequency band 1 to 10 Hz, we find transient surface wave events, an example of  
 262 which is shown in Figure 4. In this example, the wave train is travelling approximately parallel  
 263 with the fibre from 0 m to 1 km, with an apparent velocity around 1.8 km/s, close to the surface

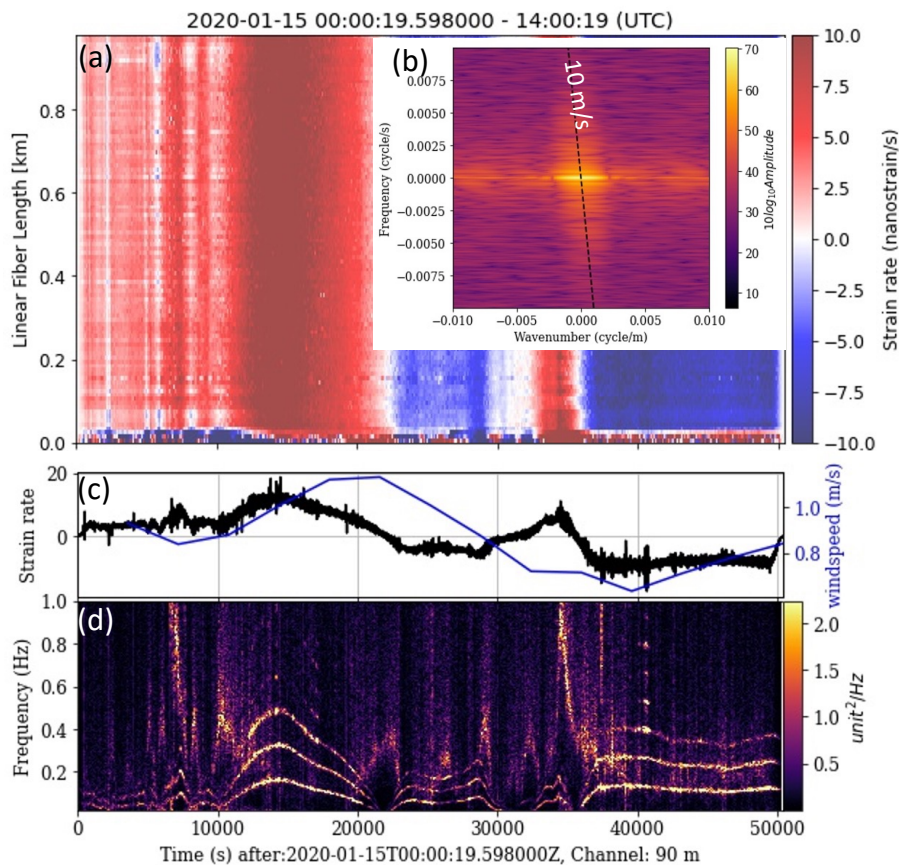
264 wave velocity below 10 Hz, as will be shown in Section 5 (Figure 9). But it is difficult to locate  
 265 this event from the 1D DAS array. The dispersion behaviour of the signal is clearly shown in the  
 266 spectrogram in Figure 4c. More than 2000 such events are detected on the 2D geophone array  
 267 from one month of recording. Using differential travel-times across the geophone array  
 268 calculated from cross-correlations, 248 of such events are located and reported in the  
 269 supplementary information (Figure S2). They appear to originate from the shear margin of the  
 270 glacier. In this manuscript, we refer to these as 'crevasse events', bearing in mind that it may not  
 271 be accurate and the exact sources of these signals have not been resolved in the study, but  
 272 crevasse and ice fractures at and beyond the shear margins are two potential candidates. Similar  
 273 signals have contributed to ambient noise analysis at an alpine glacier (Walter et al., 2015, 2020).



274  
 275 *Figure 4. An example surface wave signal from a presumable crevasse event. (a) Ten seconds of DAS measurement after*  
 276 *median removal and bandpass filter 1 to 10 Hz, with amplitude represented in colour saturated between -1 and 1 nanostrain/s.*  
 277 *(b) Time series for the DAS channel at 40 m. (c) Spectrogram of channel 40 m calculated from FFT with a 2-second sliding*  
 278 *window*

279 3.3 Wind-correlated signals ( $< 1$  Hz)

280 For data below 1 Hz, we find coherent signals with periods longer than 100 seconds  
 281 (lower than 0.01 Hz) (Figure 5a). These signals are mostly travelling towards 0 m along the DAS  
 282 cable and have propagating speeds of the order of 10 m/s, as shown in the f-k domain (Figure  
 283 5b). In the frequency band 0.1 to 1 Hz, there are signals that oscillate at 3 isolated frequencies  
 284 (Figure 5d). Interestingly, when comparing amplitude in Figure 5c with frequencies in Figure 5d,  
 285 there seems to be a correlation: the higher the strain rate below 0.01 Hz, the higher the oscillation  
 286 frequency between 0.1 to 1 Hz (e.g., from 10000 s to 20000 s). Although the correlation does not  
 287 always hold.



288  
 289 *Figure 5. Low frequency signals recorded by DAS (after a 1 Hz low pass filter). (a) 14 hours DAS recording, with amplitude*  
 290 *represented in colour saturated between -10 and 10 nanostrain/s. (b) The f-k transform of the first 10000 seconds of DAS data.*

291 *(c) The waveform at channel 120 m and predicted windspeed by the European Centre for Medium-Range Weather Forecasts*  
292 *(ECMWF) at location (84W 78.1S). (d) Spectrogram of channel 120 m calculated from FFT with a 100-second sliding window.*

293 To investigate the origin of these coherent signals, we compare the waveform with the  
294 meteorological forecast model from ECMWF--European Centre for Medium-Range Weather  
295 Forecasts, (2017). We find a correlation between the 1 Hz low-passed waveform and windspeed  
296 prediction (Figure 5c), i.e., the higher the wind speed, the higher the strain rate. It might suggest  
297 that wind-induced pressure variation on the ice surface was sensed by the optical fibre. In  
298 addition, wind-induced air oscillation may be the source of the oscillating signal from 0.01 to 1  
299 Hz. We observe that the oscillation signals from 0.01 to 1 Hz have no spatial coherence when  
300 looking at the f-k domain (Figure S1d), which might suggest they are caused by the direct impact  
301 of the wind. Additionally, in the cross-correlations (Figure 6b), we also see the strain signal of a  
302 moving marker-flag driven by the wind, although that signal is higher in frequency (9 Hz).  
303 Although these explanations are somewhat speculative, they all point to the same cause: wind. It  
304 is thus concluded that the shallow buried cable still measures mostly wind-correlated noise  
305 below 1 Hz, although it has a better coupling and a lower noise level compared with unburied  
306 cable (Hudson et al., 2021). Our observations suggest that including weather measurements such  
307 as wind speed and direction might be helpful with interpretation of future seismic acquisitions  
308 with DAS.

## 309 **4 Seismic Noise Interferometry**

### 310 4.1 Cross-correlation interferometry

311 Since the work of Shapiro et al. (2005) and Shapiro & Campillo (2004), seismic noise  
312 interferometry (SI) has become a well-established technique to probe subsurface seismic  
313 properties, especially with surface waves derived from ambient microseism noise (Bensen et al.,

314 2007; Shapiro et al., 2005; Shapiro & Campillo, 2004). It is termed seismic noise interferometry  
 315 as the method utilizes continuous seismic records without specifying their sources (location and  
 316 origin time) and assuming it is random and azimuthal-isotropically distributed. An extensive  
 317 literature review of the subject is provided by Snieder & Larose (2013). In this paper, we term  
 318 the records as ‘signals’, especially when we investigate their characters. But when applying  
 319 seismic interferometry, coherent seismic signals and noise are collectively referred as ‘seismic  
 320 noise’ and we do not specifically distinguish them.

321 Recent studies have implemented SI with DAS data in a borehole (Lellouch et al., 2019),  
 322 submarine (Cheng et al., 2021; Spica, Perton, et al., 2020), and urban environment (Ajo-Franklin  
 323 et al., 2019; Dou et al., 2017; Spica, Perton, et al., 2020). Most of those studies calculate  
 324 interferogram by cross-correlation (CC) with a ‘virtual source’ at one DAS channel and then  
 325 apply stacking to enhance coherent signals. This is adopted from the workflow for processing  
 326 conventional seismometers or geophones data. We also adopt this workflow, and a detailed  
 327 processing flow is presented in Figure S3.

328 Firstly, we slice the continuous data into small segments in the time-domain, then we  
 329 calculate the spectrally whitened CCs:

$$330 \quad c_i(\omega) = \frac{1}{N} \sum_{n=1}^N \frac{r_i(\omega)s(\omega)^*}{\sqrt{r_i(\omega)^2 s(\omega)^2}}, \quad i = 1, 2, \dots, m$$

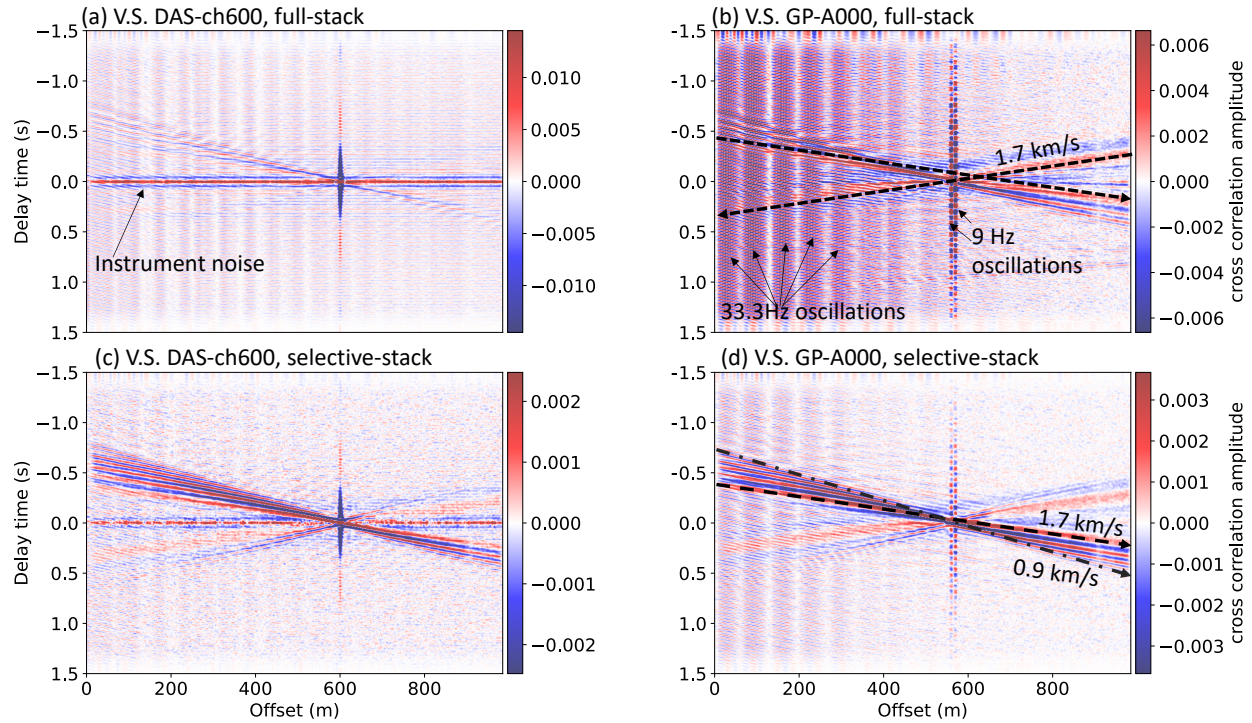
331 For each segment  $n$ , we decimate the sampling rate to 200 Hz, then apply a tapered cosine. A  
 332 Fourier transform is applied for each channel, so the virtual source channel and each receiver  
 333 channel are represented in frequency-domain:  $s(\omega)$ ,  $r_i(\omega)$  ( $m = 1000$  for the linear DAS array).  
 334 Since the desired seismic noise is above 1 Hz, we choose a segment length of 10 seconds, with

335 an overlap of 5 seconds. To keep the process simple, we do not apply time-domain normalization  
336 (1-bit) or remove the basal icequakes signals before CCs. While The power spectra,  $r_i(\omega)^2$  and  
337  $s(\omega)^2$ , are smoothed by a 21-sample moving average, a process known as spectral whitening.  
338 The cross-correlations over each segment  $c_i(\omega)$  are stacked over every 2 minutes. These 2-  
339 minutes CCs are stored for further processing.

340 Although the ‘CC-stacking’ workflow is applied here, we note that to directly retrieve  
341 surface wave dispersion data, we could stack data in the frequency-wavenumber (f-k) domain,  
342 without calculating CC (e.g., Cheng et al., 2019; Spica, Nishida, et al., 2020). But, after f-k  
343 domain stacking, phase information is lost, and the data cannot be converted back to the time  
344 domain for inspection or further analysis.

#### 345 4.2 Choice of virtual source: DAS versus geophone

346 DAS interferogram profiles are obtained through linearly stacking 2-minute CC panels  
347 over the entire recording period of five days (Figures 6 a & b). We produce two different  
348 interferograms. The first uses the DAS channel at 600 m as a virtual source (Figure 6a), while  
349 the second takes the vertical component of a co-located geophone, at offset ~570 m, as the  
350 virtual source (Figure 6b). In Figure 6a, we see the CCs (DAS virtual source) have the highest  
351 amplitude at 0 s delay time, which is due to coherent DAS instrument noise (Figure S1e), while  
352 the seismic responses, especially at a lower frequency and larger distance, are faint.



353

354 *Figure 6. CCs (1 – 30 Hz, 2<sup>nd</sup> order butter bandpass zero-phase filtered) from 4 approaches. (a) Stacked cross-correlations, a*  
 355 *virtual shot gather, with a virtual source at DAS channel at 600 m. (b) Same as (a) but with a virtual source at a geophone*  
 356 *(A000) located close to channel 570 m. (c) Selective-stacked CCs for the same data as (a). (d) Selective-stacked CCs for the same*  
 357 *data as (b). Note for each panel, the colour scale is saturated at the median over maximal values from each channel for*  
 358 *visualization.*

359

360

361

362

363

364

365

366

367

In the second approach (Figure 6b), a geophone is used as the virtual source to cross-correlate with DAS channels, which we term hybrid instrumenting CC. A clearer CC profile is retrieved, and the 0 s delay time instrument noise is completely erased. The seismic signals become clear, and we can see that they are travelling both forward (from 0 m to 1 km along the cable) and backward with an apparent velocity of  $\sim 1.7$  km/s. Its dispersive nature shows that it is a surface wave. Since DAS records longitudinal strain along the fibre, parallel to the propagation direction of the retrieved signal, this surface wave is classified as a Rayleigh wave. The Rayleigh wave response between the vertical component geophone and the horizontal component DAS is the result of elliptical particle motion in the vertical plane, parallel to the direction of

368 propagation. We have tested the process with the horizontal component (East, near parallel to the  
369 DAS cable) of the geophone, which showed little difference in terms of signal quality.

370 Figure 6b shows features such as the high frequency (33.3 Hz) oscillating noise that  
371 decays away from the start of the line at 0 m. This strong harmonic signal is generated by the  
372 petrol generator (Figure 3c). There is also strong 9 Hz oscillation noise around 560 and 570 m,  
373 which is likely strain produced by the wind-driven movement of the poles of two marker-flags  
374 (used to indicate the location of the geophones). Since this 9Hz noise is very localized, it does  
375 not influence further analyses.

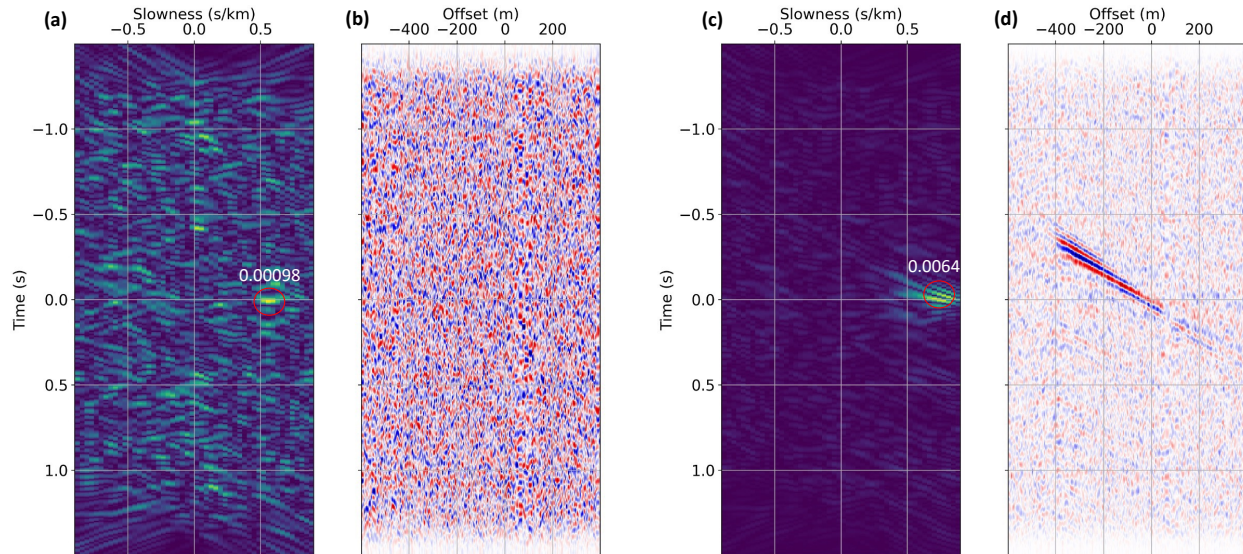
#### 4.3 Selective stacking of cross-correlations

376 To improve the quality of the final interferogram image, previous studies have introduced  
377 more sophisticated techniques of stacking CCs, such as phase-weighted stacking (Schimmel et  
378 al., 2011; Schimmel & Paulssen, 1997) and SNR-weighted stacking (Cheng et al., 2015). The  
379 phase-weighted stacking suppresses incoherent noise between two CCs and has several  
380 advantages over a standard linear stack (Dou et al., 2017). This approach, however, assumes that  
381 coherent seismic noise is continuous over each time span of CCs. In our case, most of the  
382 seismic signal recorded in our dataset are transient in nature; an exception is the harmonic signal  
383 from the generator. SNR-weighted stacking is based on the SNR of CCs and has been shown to  
384 perform well for anthropogenic seismic noise above 2 Hz, which are often transient and spatially  
385 variable (Cheng et al., 2015). Manual inspection of our 2-minute CCs shows that some retrieved  
386 Rayleigh wave signals have very low SNR on individual channels. Such CCs would be down-  
387 weighted if applying SNR-weighted method. However, these weak Rayleigh wave signals are  
388 visible because of their spatial coherency, which inspired us to use spatial coherency to detect  
389 and select data containing Rayleigh wave signals.

390           The studies on anthropogenic noise interferometry by Zhou & Paulssen, (2020)  
391 introduced a pre-processing step by detecting and extracting noise, such as trains, for stable time-  
392 lapse CCs. That approach, however, requires a sophisticated detection scheme. Cheng et al.  
393 (2019) applied tau-p transform on processed time domain data and selected segments based on  
394 an SNR defined from the distribution of slowness ( $p$ ).

395           Rather than selecting from the raw data, a CC-based selection scheme is computationally  
396 cheaper. Previous noise interferometry studies have selected CCs before stacking based on SNR  
397 (Olivier et al., 2015), amplitude decay (Dou et al., 2017), and apparent velocity from 2D array  
398 beamforming analysis (Vidal et al., 2014). We term these CC selection schemes as selective  
399 stacking.

400           For the linear DAS array, applying the linear tau-p transform (slant-stack) (Diebold &  
401 Stoffa, 1981) could highlight spatially coherent signals which have a near straight-line moveout.  
402 We thus applied tau-p transform to each 2-minute CCs panel for the frequency band 3 to 25 Hz.  
403 Following a manual inspection of the tau-p diagrams (two examples are shown in Figure 7), we  
404 find the tau-p domain maximal amplitude is a sufficient and easy to apply criteria. For CCs  
405 between geophone and DAS, we set the criteria as follows: (1) maximal amplitude is not lower  
406 than 0.0014 (CC coefficient), (2) maximum locates at delay time close to zero ( $0 \pm 0.05$  s), and  
407 with an apparent velocity smaller than 2500 m/s (slowness  $< -0.4$  or  $> 0.4$  s/km).



408

409 *Figure 7. Examples of tau-p transform of CCs. (a, b) Example of a noisy CC panel, with peak amplitude in the tau-p domain*410 *0.00098. (c, d) Example of a selected CC panel, with tau-p domain peak amplitude 0.0064.*

411 These two criteria allow the selection of CCs containing clear surface wave signals. The  
 412 example in Figure 7a, shows a slowness larger than 0.4 s/km and delay time close to zeros, but  
 413 the maximal amplitude (0.00098) is much smaller than 0.0014, therefore this CC panel is not  
 414 selected. The strong signal shown in Figure 7c meets the criteria and is therefore selected.

415 For the 3068 (5 days with few hours of data loss) 2-minute CC panels, 453 met the  
 416 selection criterion and were linearly stacked. The selective-stacked CCs are presented in Figure  
 417 6c & d, and show much higher SNR of seismic responses compared to those for the non-  
 418 selective stacked CCs (Figure 6a & b). Although for a DAS virtual source (Figure 6c), the  
 419 coherent instrument noise is still present in the selectively stacked CCs, the seismic response is  
 420 clearer since a large component of instrument noise is removed.

421 We achieve the best quality CCs for this dataset by combining a geophone as virtual  
 422 source and selective stacking (Figure 6d). A signal shows clear dispersion as the higher  
 423 frequency signals have a steeper slope, which indicates a slower velocity.

## 424 **5 Dispersion and 1D velocity structure**

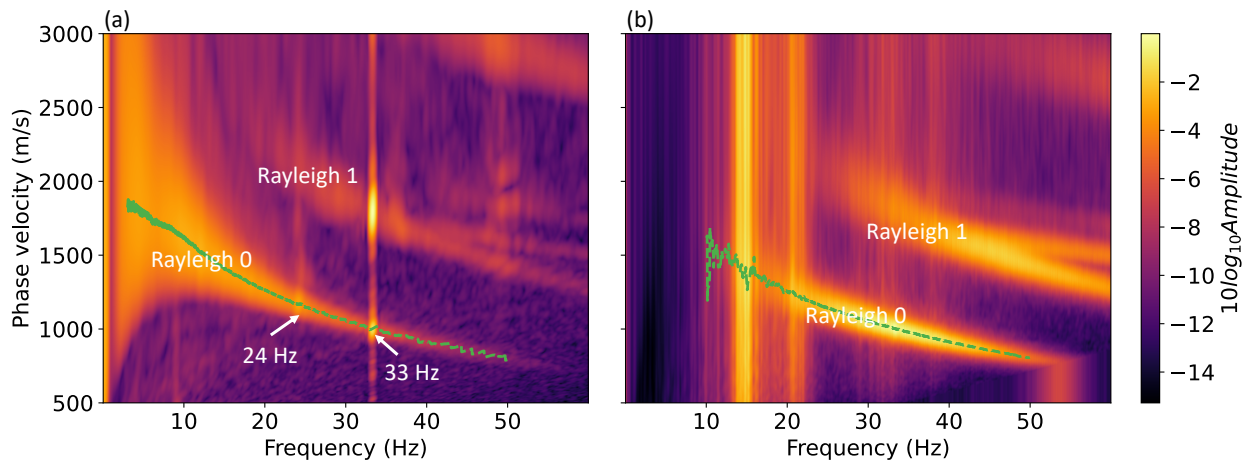
### 425 5.1 Dispersion analysis

426 Surface wave phase velocity dispersion curves can be extracted in the frequency-velocity (f-v)  
427 domain which can be achieved with a frequency-wavenumber (f-k) transform, or through  
428 sweeping slant stack or tau-p transform for narrowly band-passed multichannel data (Xia et al.,  
429 2007). Such an approach is often termed multichannel analysis of surface waves (MASW) (Park  
430 et al., 1999; Xia et al., 1999), or PMASW for passively retrieved surface waves from CC (Cheng  
431 et al., 2016). In this study, a 2D Fourier transform (f-k transform) is applied after tapering the  
432 CCs with a Hann window in both the time and space dimensions. We further stack the positive  
433 and negative parts of the wavenumber domain to enhance the signal. These f-k diagrams (Figure  
434 S4) are then converted to the frequency– phase velocity (f-v) domain (e.g., Figure 8a). Multiple  
435 modes of Rayleigh waves are present in both datasets, but for simplicity, only the fundamental  
436 mode dispersion curve is extracted by picking the local maximal amplitude.

437 For comparison, we also analysed an active dataset. Data were collected from 21 shot  
438 locations (2 or 4 shots for every 50 m) using a sledgehammer source. This survey is processed to  
439 produce a frequency-velocity plot, which is similar to that obtained from the CCs. For each shot  
440 gather, DAS channels are split into two sides by the location of the active source. The f-k  
441 transform is separately applied to both sides to avoid interference. Then, the data are stacked in  
442 the f-k domain: (1) for each f-k diagram, the negative and the positive wavenumbers are stacked.  
443 (2) for each shot gather, the two f-k diagrams are stacked. (3) for all shot gathers, they are further  
444 stacked to produce a single f-k diagram. Lastly, the f-k diagram is converted the f-v domain  
445 (Figure 8b).

446           The fundamental mode (Rayleigh 0) and the first higher mode (Rayleigh 1) from both the  
447 passive CCs and the active sources are shown in Figure 8. In general, there is strong agreement  
448 between the two approaches in the frequency range 15 to 50 Hz. Figure 9 shows the extracted  
449 Rayleigh 0 dispersion curves, showing a good agreement between the two approaches. This  
450 provides us with confidence that the methods adopted when producing the noise interferograms  
451 are appropriate. The passive dataset contains relatively lower frequency signals, and its  
452 dispersion curve is well constrained down to 3 Hz (Figure 8a). From Figure 8b, we see that the  
453 stacked active shots data contain signals mostly above 10 Hz with dispersion most stable  
454 between 15 and 50 Hz. This is likely due to the lack of low-frequency energy generated by the  
455 hammer and plate source, compared to ambient seismic noise. At around 33.3 Hz, there is a  
456 small but sharp reversal of velocity from the CCs derived dispersion (Figure 8a), which is due to  
457 the near-constant wavenumber of the strong noise observed at 33.3 Hz (Figure 3d and Figure 6).  
458 The strong signal causes spectral leakage in fast Fourier transforms (FFT) even though a Hann  
459 window taper was applied before the FFT. However, it does not influence our inversion as the  
460 frequency range is small.

461



462

463 *Figure 8.* Extracting Rayleigh wave fundamental mode (Rayleigh 0, green dashed lines) dispersion curve from the frequency-  
 464 velocity domain, by picking the local maximum amplitude. (a) Frequency-velocity plot of the stacked CCs. The Rayleigh 0 mode  
 465 dispersion curve is extracted from 3 to 50 Hz. Note, that *two oscillatory* signals are present at 24 and 33 Hz. (b) Stacked  
 466 frequency-velocity plot of the 21 active shots. The Rayleigh 0 mode is extracted from 10 to 50 Hz.

## 467 5.2 Velocity inversion

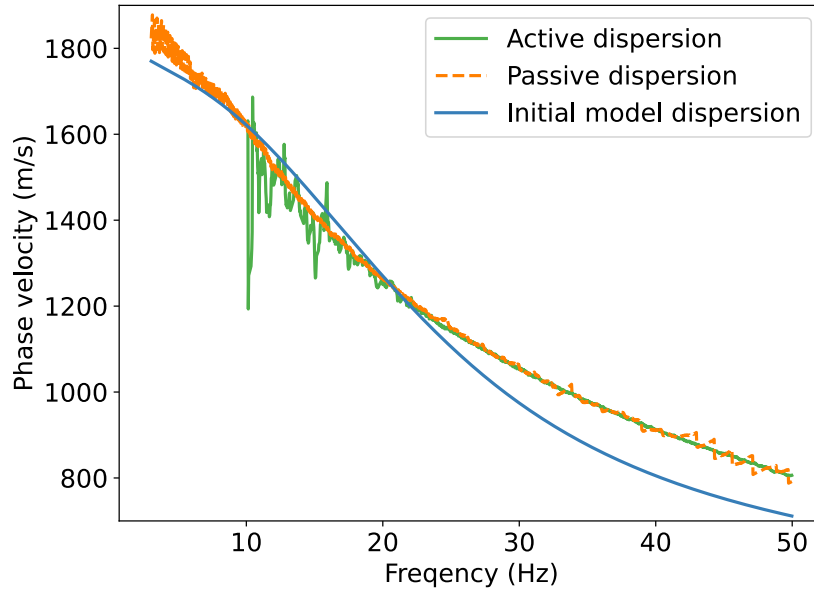
468 Most previous surface wave inversion studies treat the subsurface as a layered model  
 469 with either fixed or variable layer thickness (for two-station (Yudistira et al., 2017) or multi-  
 470 station (Cheng et al., 2015; Xia et al., 1999) surveys). The firm layer is defined as a layer with  
 471 continuous metamorphism of snow to ice, which results in a smooth increase of P- and S-  
 472 velocity and density as a function of depth (King & Jarvis, 2007; Schlegel et al., 2019), until it  
 473 becomes near constant beneath  $\sim 100$  m at Rutford Ice Stream. We therefore use a near-  
 474 continuous model of 100 layers, each with a layer thickness of 1 m, overlying on a half-space at  
 475 the bottom of the model.

476 To simulate the phase velocity dispersion of the Rayleigh wave, we use the Python  
 477 package *disba* (Luu, 2021), which was translated from the well-adapted Fortran program *surf96*  
 478 from Computer Programs in Seismology (Herrmann, 2013). With a 100-layer model, we

479 significantly increase the number of variables and the non-uniqueness of the inversion. A  
480 Gaussian-Newton inversion procedure is applied using the package pyGimli (Rücker et al.,  
481 2017), with the regularization lambda to be 20, and a predefined relative error of 10% to prevent  
482 overfitting. The large relative error and regularization also means that we find a solution which is  
483 close to the starting model.

484 To prepare a realistic starting model, we applied the WHB inversion to the refraction data  
485 set acquired by Smith et al. (2015) to obtain a  $V_p$  model (Figure 1c). Then assuming a constant  
486  $V_p/V_s=1.95$  (Smith et al., 2015), we obtained a  $V_s$  model. We name this model the ‘standard  $V_s$ ’  
487 and use it as a comparison to our surface wave inverted models. The starting model for the  
488 inversion is a smoothed version of the standard  $V_s$ . The general trend of the standard  $V_s$  model is  
489 preserved but the ‘kink’ at around 9 m is smeared (Figure 10 a). Figure 10b highlights the  
490 differences between the standard  $V_s$  model and the starting model, which shows that the standard  
491  $V_s$  model has a higher value from 0 m to ~25 m and lower value from ~25 m to 100 m.

492 Figure 9 shows that the starting model is generally consistent in phase velocity dispersion  
493 with that obtained from the data. At higher frequencies, the starting model has lower phase  
494 velocity than the data, which indicates the starting model underestimates the phase velocity at  
495 shallow depths.



496

497 *Figure 9. Comparing observed (CCs and active shots) with initial model dispersion curves, from 3 to 50 Hz. The initial Vs model is*  
 498 *presented in Figure 10.*

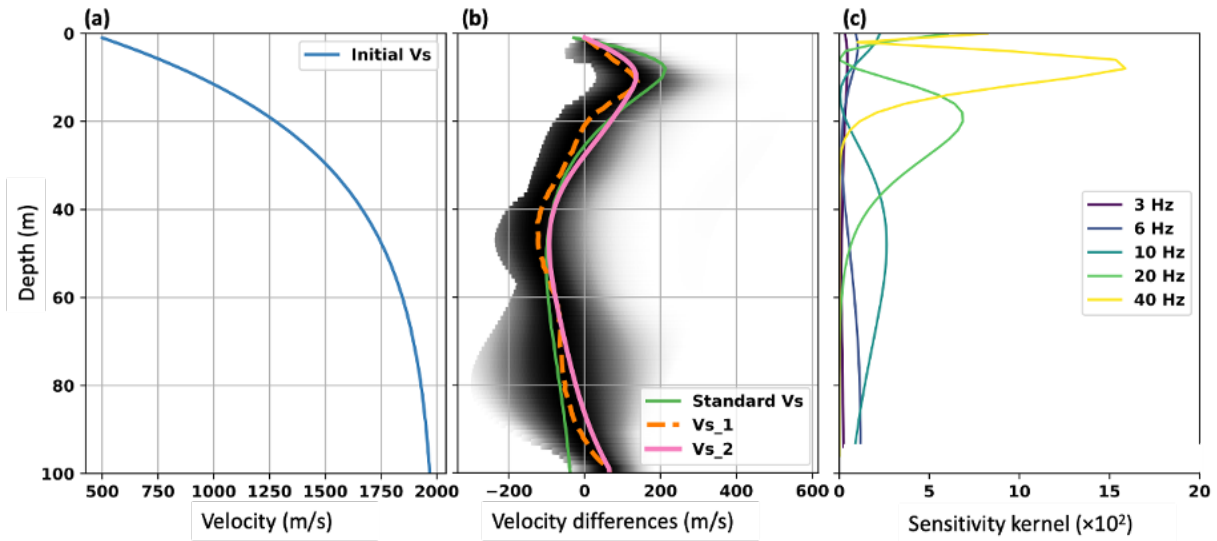
499 To capture the uncertainty in the data, we calculate the CCs for 3 geophones (1 co-  
 500 located, and 2 in-line with the DAS cable). For each virtual source, we produce 9 dispersion  
 501 curves, by dividing the 453 selected CCs into 9 groups for stacking. This process results in 27  
 502 (9×3) dispersion curves (Figure S5). We then invert all 27 dispersion curves for S-wave velocity  
 503 profiles. Lastly, a probability density function (PDF) is calculated for each layer over its 27  
 504 measurements. The maximal point of PDFs, for each layer, represents a final Vs profile (Vs\_1).  
 505 In Figure 10 b, we present the inverted Vs\_1 after subtracting the starting model, with the  
 506 amplitudes of PDFs presented as greyscale. See Figure S3 for further details of the process.

507 Alternatively, Vs Figure 10 is directly inverted from the dispersion curve in Figure 9  
 508 (Vs\_2 in Figure 10b), which is from the fully stacked CCs (all the 453 selected time spans and 3  
 509 virtual sources).

510 As highlighted in Figure 10b, the  $V_s$ \_1 profile is almost overlapping with the  $V_s$ \_2  
511 profile from 0 to 14 m, while the two profiles differ slightly at depths below 14 m, which further  
512 indicates uncertainties of the final models. In general, our two  $V_s$  models agree with the standard  
513  $V_s$  down to 80 m depth. Below 80 m depth, our models suggest a slightly steeper increase in  
514 velocity compared to the standard  $V_s$ , reaching up to 100 m/s higher than the initial model. In  
515 both our  $V_s$  models and the standard model, we see a clear peak (largest difference with the  
516 initial model) at around 9 m (standard  $V_s$ ) to 12 m ( $V_s$ \_1) depth, which is similar to the  
517 densification observation and modelled by the regional atmospheric climate model by van den  
518 Broeke (2008), across West Antarctica.

519 Sensitivity analysis is done at discrete frequencies (3, 6, 10, 20, 40 Hz) as shown in  
520 Figure 10c using the inverted  $V_s$ \_1 model. This indicates that the highest sensitivity of most  
521 signals ( $> 20$  Hz) is over the 0 to 40 m depth range. Signals below 10 Hz have greater sensitivity  
522 over the lower part of the model. Below 6 Hz, the Rayleigh wave is dominantly sensitive to the  
523 lowermost layer of our model, which is assumed to be a half-space.

524



525

526 *Figure 10. (a) Initial smooth Vs model. (b) Velocity difference between Inverted Vs models and the initial model, Vs\_1 from maximal*  
 527 *PDF (greyscale) and Vs\_2 from direct inversion of a fully selective stacked CCs virtual shot gather. The Vs profile derived from the*  
 528 *standard Vp refraction experiment is shown in green. (c) Sensitivity kernel calculated from the inverted model Vs\_1.*

529

### 5.3 Is the firn layer seismically anisotropic?

530

Clear azimuthal anisotropy has been reported at Rutford Ice Stream by Harland et al.

531

(2013) and Smith et al. (2017), with the fast S-wave direction perpendicular ( $90^\circ$ ) to the ice flow

532

direction (IFD). Hudson, Baird, et al. (2021) also observed strong shear wave splitting in

533

icequake signals recorded by DAS. These seismic experiments do not provide constraints on the

534

depth distribution of the anisotropic ice, as the measurements integrate over the entire wave path

535

from the icequake hypocenter (ice-bed interface) to the surface receivers. However, using

536

polarimetric radar measurements, Jordan et al (2022) report near-surface azimuthal anisotropy on

537

Rutford Ice Stream, although their measurements are not coincident with this experiment.

538

We investigate the feasibility of imaging anisotropy with surface waves retrieved from a

539

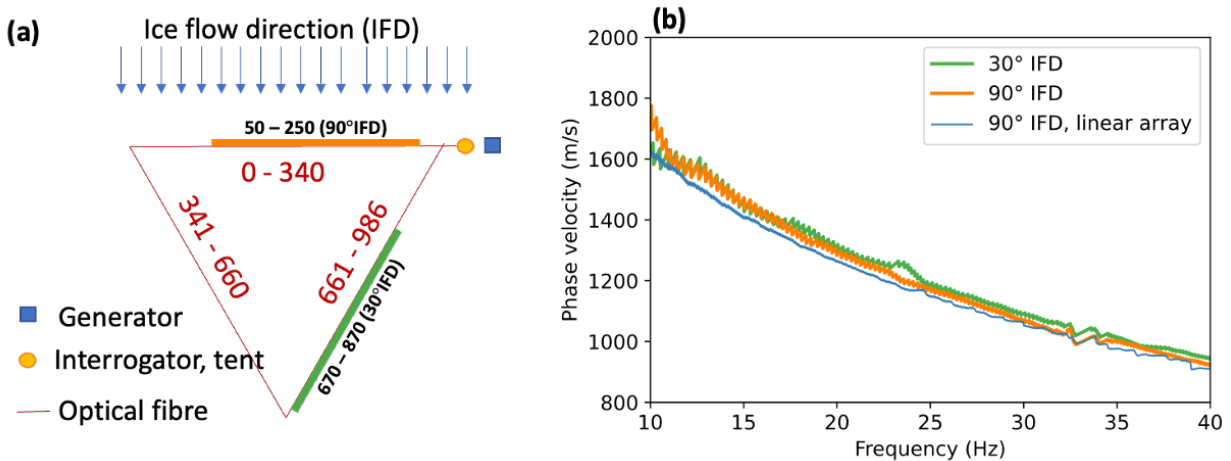
different azimuth on CCs. For this, we use a DAS array arranged in a triangular configuration

540

and assume a laterally homogenous firn layer. As shown in Figure 11a, we take two segments of

541 the triangular array (channel 50-250 and channel 670-870). We chose channels 670-870, with a  
542 larger distance to the tent and the generator, to reduce the angle between the ray path and the  
543 DAS cable. Since the snowmobile traveling from the tent to the generator is the dominant high-  
544 frequency seismic noise source, we could not retrieve a stable Rayleigh wave response from the  
545 third segment that is perpendicular to the wave propagation direction.

546 With virtual sources at DAS channels 150 and 750, respectively, we calculate and  
547 selectively stack CCs for each segment (Figure S6). A higher selection threshold of 0.01 is  
548 chosen as the DAS CCs are in general of higher amplitude than DAS-geophone CCs. Dispersion  
549 curves of the 2 segments are then calculated from the f-k domain (Figure S6), as with the linear-  
550 array study. In Figure 11b we show the two dispersion curves together with the result from the  
551 linear array. Note the linear array result is more stable due to the involvement of geophone data.  
552 The difference between the triangle array 90° IFD dispersion curve and the linear array result  
553 might indicate a slight horizontal heterogeneity in the firn layer. Horizontal heterogeneity might  
554 also exist between the two sides of the triangle. When comparing the two dispersion curves from  
555 the triangle array we see that they are in general nearly overlapping with each other from 10 to  
556 27 Hz. For above 27 Hz, the 30° IFD curve indicates a slightly higher phase velocity, but the  
557 difference is small compared with the measurement uncertainties. Note that around 24 Hz and 33  
558 Hz, there are artefacts from the f-k transform. In this study, neither the heterogeneity- nor the  
559 anisotropy-effect produces a notable dispersion curve difference between the 30° IFD and 90°  
560 IFD. Thus, it suggests that the firn layer, above ~80 m depth (for the signals above 10 Hz), is  
561 likely not strongly azimuthally anisotropic. We note that our measurements here have large  
562 uncertainty and that we cannot rule out a VTI anisotropy in the firn layer. A comparison of  
563 Rayleigh and Love wave derived shear-velocities would provide a means of testing this.



564

565 *Figure 11. (a) Schematic of the geometry of the triangle DAS array, with a loop of 986 m. The thick lines indicating two 200 m*  
 566 *DAS segments have been used for the ANI study. (b) Dispersion curves were obtained from the two segments which are close to*  
 567 *the tent indicated as 90 o IFD (ice flow direction) and 30 o IFD. The result from the linear array is also plotted.*

## 568 6 Discussions

569 In this study, we investigate the use of noise data recorded by DAS, deployed on Rutford  
 570 Ice Stream, West Antarctica, to obtain a high-resolution shear wave velocity profile of the firn.  
 571 We compare CCs calculated over five days using a single DAS channel as a virtual source versus  
 572 using three geophones (collocated or near collocated) as the virtual sources. A superior SNR is  
 573 obtained with a geophone. The coherence of instrument noise over all the DAS channels  
 574 degrades the cross-correlations, while introducing a geophone as a virtual source breaks down  
 575 that coherence of the instrument noise.

576 Stable Rayleigh wave responses are retrieved from CCs between vertical component  
 577 geophone data and horizontal component DAS data, as a result of the Rayleigh wave elliptical  
 578 particle motion. We notice, however, that there are phase shifts introduced by: (1) the ellipticity  
 579 produces a 90-degree phase shift between vertical and horizontal particle motions, (2) the  
 580 difference between particle motion velocity and strain rate, and (3) the difference in instrument

581 responses. However, these are not a problem for the dispersion analysis, as it only uses the slopes  
582 for calculating dispersion curves. We note that for studying waves other than Rayleigh waves, it  
583 might be beneficial to consider using the horizontal component parallel with the cable. We  
584 deliberately chose to use the vertical component to demonstrate the applicability of the hybrid  
585 instrument approach, because vertical component geophones are widely used for near-surface  
586 imaging applications

587         The noisy Rayleigh wave response from using a DAS channel as a virtual source is likely  
588 due to the instrument noise on DAS channels having a destructive impact on the CCs. Firstly, we  
589 can see clear horizontal bands in Figure 6a which are most dominant at  $t = 0$ , which therefore  
590 indicates that the instrument noise on each DAS channel is not independent. This is likely due to  
591 the nature of DAS measurement that senses the entire cable with a single interrogator unit, which  
592 results in such common mode noise (Lindsey et al., 2020), as shown in Figure S2.d. When a  
593 geophone is used as the virtual source, it breaks the coherency of this instrument noise.  
594 Additionally, we observe that the dominant seismic noise contributing to the seismic responses is  
595 transient in nature, therefore a large number of CCs derived from a DAS virtual source contain  
596 only instrument noise.

597         Based on our results we argue that deploying DAS together with conventional seismic  
598 instruments (hybrid instrumentation) would open more opportunities. This is consistent with  
599 previous studies, such as: combining seismometer and DAS for calculating receiver function and  
600 surface wave dispersion (Yu et al., 2019); converting strain to particle velocity or calibrating the  
601 conversion (Lindsey et al., 2020; Porritt et al., 2022; van den Ende & Ampuero, 2021), or to  
602 apply the H/V method between DAS and vertical component of a seismometer (Spica, Pertou, et  
603 al., 2020).

604 Selective stacking is applied to improve CCs. Only 453 out of 3068 2-minute CCs panels  
605 are selected and stacked for shear wave inversions. With selective stacking, we eliminate a large  
606 chunk of data containing only instrument noise. The selected CCs contain mostly high-frequency  
607 signals from the snowmobile or transient low-frequency surface wave events. The snowmobile  
608 was used to approach the generator location in-line with the linear fibre optic cable array, 50 m  
609 away from the interrogator (Figure 11a), which produces a surface wave noise travelling along  
610 the fibre. The (suspected) crevassing generated surface wave signals are mostly from the shear  
611 margin of the ice stream (Figure S2), although not homogeneously distributed, they are generally  
612 in-line with the fibre optic cable.

613 The dispersion curves obtained from the passive and active datasets show strong  
614 agreement over the frequency range 10 to 50 Hz. While the hammer and plate source surveys  
615 produce energy down to 10 Hz, it is most stable above 15 Hz, which could provide a reliable S  
616 velocity profile down to ~60 m (Figure 10). The seismic noise interferometry extends the reliable  
617 measurement range down to 3 Hz, which enables an inversion over the entire column of the firm  
618 layer.

619 We did not observe clear ocean wave-related primary or secondary microseism noise as  
620 the dominant ambient noise on broadband seismometers from 0.01 to 1 Hz (Bensen et al., 2007).  
621 Previous studies with submarine DAS cables have recorded the microseism from 0.2 to 2 Hz  
622 (Sladen et al., 2019) and down to 0.5 Hz (Cheng et al., 2015; Spica, Nishida, et al., 2020). Some  
623 onshore studies also suggest the abundance of low-frequency noise with noise power spectrum  
624 analysis (Hudson et al., 2021; Lindsey et al., 2020a). It is, however, shown in our study that the  
625 DAS signals below 1 Hz are likely wind-related, which could due to shallow burial depth of the

626 cable. It is also possible that the linear fibre is insensitive to microseism signals because of its  
627 propagation direction near perpendicular to the fibre.

628         The S-wave velocity profile obtained from this study fits well with the velocity profile  
629 which we inverted from a standard refraction P-wave experiment conducted in the BEAMISH  
630 project (Smith et al., 2021), assuming a  $V_p/V_s$  ratio of 1.95 (Smith et al., 2015) at depths of 0 to  
631 80 m. Below 80 m the profiles from the methods diverge, with higher  $V_s$  at depths greater than  
632 80 m from the surface wave inversion. This may suggest a decrease of the  $V_p/V_s$  ratio at depth,  
633 or an increase in azimuthal anisotropy. However, at these depths, the reliability of the standard  
634 refraction results decreases due to the data offset limitation of  $\sim 1$  km. Also, spatial heterogeneity  
635 cannot be ruled out as the surveys are not collocated. Nevertheless, the shape and form of the  
636 inverted  $V_s$  profiles show good agreement with the refraction survey, with both methods  
637 showing a velocity-depth gradient change at around 12 m. This feature of the velocity profile  
638 indicates the depth of the critical density, marking the transition between the first two stages of  
639 the densification process (Herron & Langway, 1980). Above this depth, the dominant  
640 compaction mechanism is grain settling and packing and exhibits the highest densification rate.  
641 Below this transition progression to pore close-off occurs with a lower rate of densification. The  
642 velocity-depth gradients above and below this depth agree with this interpretation. This  
643 agreement between the methods, reproducing the velocity gradient transition at similar depths is  
644 significant. The standard refraction WHB method uses a double exponential fit to the travel-  
645 times (Kirchner & Bentley, 1979) which can force the presence of this gradient change when a  
646 simple polynomial fitting method may not. The results from noise interferometry and surface  
647 wave inversion, therefore, verify the assumption of the double exponential fitting step at this site

648 and provide an independent and robust measure of this critical density transition in the firn  
649 profile.

650         With a triangular fibre optic array, we retrieve Rayleigh wave responses along 90° and  
651 30° from the ice flow direction. We find a small difference between the two dispersion curves  
652 from 10 to 40 Hz. Considering uncertainties in the measurements, it qualitatively indicates no  
653 strong azimuthal anisotropy in the upper 80 m (the dominant sensitivity of this frequency band is  
654 the top 80 m (Figure 10b)). However, polarimetric radar measurements of Jordan et al. (2022)  
655 indicate azimuthal anisotropy at depths of 40 to 100 m across Rutford Ice Stream. Laterally, they  
656 find weaker anisotropy strength in the ice stream central (less deformation) than in the shear  
657 margin. Our measurements of the azimuthal variation of the Rayleigh wave-phase velocity  
658 contain uncertainties that may be due to lateral heterogeneity in the firn layer or instability of the  
659 cross-correlation functions. But within that uncertainty, our measurements are consistent with the  
660 Jordan et al. (2022) results and do not suggest high azimuthal anisotropy at the centre of the ice  
661 stream.

662 Our measurements of  $V_s$  complement those of  $V_p$ , without requiring additional S wave sources  
663 or 3-component sensors. The method uses DAS, collocated vertical component geophones, and  
664 natural seismic signals from crevasses and noise from snowmobiles, which means it could be  
665 convenient for the deployment and might be a feasible method for large-scale firn imaging. This  
666 may lead to an improved understanding of the mechanical properties of the firn and their  
667 variation. Although standard refraction methods can be adapted to derive a  $V_s$  profile, with S  
668 wave sources and 3 component instruments (King & Jarvis, 2007; Kirchner & Bentley, 1990), in  
669 general, only  $V_p$  profiles are measured. Efforts were made to reproduce the standard P-wave  
670 refraction survey method using diving P-waves from a hammer and plate source with DAS

671 recording. However, inherent to the DAS method, a combination of the effects of gauge length  
672 and spatial averaging near the shot location, hinders the derivation of a high accuracy velocity  
673 profile. Nevertheless, our study suggests that DAS measurements and surface wave inversion  
674 have the potential to upscale for the investigation of firm properties over large areas.

675 Another potential benefit of the method presented here compared to the standard seismic  
676 refraction method is the capacity of the surface wave (passive or active) to image low-velocity  
677 layers (Zhang et al., 2007). The seismic refraction method would fail in the presence of low-  
678 velocity layers as no rays will undergo critical refraction at the top of it (base of the ice lens).  
679 This situation may arise where melt has occurred and refreezing produces ice lenses overlying  
680 lower velocity firm layers, as for example reported on Larsen C Ice Shelf (Ashmore et al., 2017).

681 Although the  $V_s$  profile in our study is inverted from noise CCs, we observe consistency  
682 between CC retrieved dispersion and active shot dispersion, which suggests the inversion  
683 methods would work with active seismic data as well. A source producing lower frequencies  
684 (e.g., explosives or weight drop) would allow greater depth penetration. Since Rayleigh wave  
685 signals are naturally acquired in conventional refraction surveys, revisiting these data with our  
686 method could provide an independent measurement of  $V_s$  and might yield new insights.

## 687 **7 Conclusions**

688 Applying noise interferometry to DAS data, we retrieved broadband (3 – 50 Hz) and  
689 stable CCs representing Rayleigh wave responses travelling along the DAS fibre. We show that  
690 the SNR improves when using a collocated geophone as the virtual source or selective stacking  
691 of only the best CCs (selection based on the tau-p domain). Noise sources are found to be  
692 transient including lower-frequency (2 – 10 Hz) surface wave signals from the shear margins of

693 the ice stream, and high-frequency noise up to 80 Hz from a snowmobile. The Rayleigh wave  
694 dispersion curves are validated using active shot gathers.

695 Inverting the dispersion curves, we produce an S-wave velocity ( $V_s$ ) profile of the firn  
696 layer, which resolves a ‘kink’ at 12 m depth, corresponding to the critical density where the  
697 mode of firn compaction changes. This model shows good agreement with a standard  $V_p$   
698 refraction derived model. No significant azimuthal anisotropy is observed in the upper 80 m,  
699 using 10 to 40 Hz signal, which is consistent with previous studies that along the centre of the ice  
700 stream the top of the firn layer is not under strong horizontal deformation.

701 Our study demonstrates that the usage of surface waves, retrieved from DAS seismic  
702 noise interferometry, could complement the refraction  $V_p$  profiles, for studies of the firn layer.  
703 Since the acquisitions of DAS and seismic noise are simpler than geophone refraction surveying,  
704 these measurements have the potential to upscale to large areas of the ice sheets. This in turn  
705 might help decrease the uncertainty of mass balance estimation and palaeoclimate studies.  
706 Additionally, using surface waves instead of refraction waves will potentially allow investigation  
707 of the firn column where standard refraction methods fail in the presence of low velocity layers,  
708 such as have been observed on lower-latitude ice shelves. Finally, the methodology that we have  
709 developed can be easily applied to imaging the near surface in a host of other environmental  
710 applications where fibre optic cables can be deployed; examples include landslide monitoring,  
711 levee and embankment assessment, and sinkhole studies.

## 712 **Acknowledgements**

713 This work was funded by the UK’s Department for Business, Energy and Industrial  
714 Strategy through the DigiMon ACT CCS project (project number 299622), and the NERC

715 Collaborative Antarctic Science Scheme grant (grant number CASS-166). Fieldwork was  
716 undertaken as part of the BEAMISH Project (NERC AFI award numbers NE/G014159/1). We  
717 thank Silixa for the loan of an iDAS interrogator. Geophones were borrowed from the UK  
718 Geophysical Equipment Facility (GEF loan number 1111). Obspy (Krischer et al., 2015) is  
719 intensively used for data processing. The tau-p transform was performed with PyLops (Ravasi &  
720 Vasconcelos, 2020). Jelle Assink (KNMI) is thanked for useful discussion on the low-frequency  
721 signal in DAS and pointing out the weather data from ECMWF. Thomas Hudson, Sacha Lapins  
722 are thanked for useful discussions. Hanneke Paulssen is thanked for reading and commenting the  
723 manuscript. We thank Emma Smith and other two anonymous reviewers for their constructive  
724 comments.

## 725 **Open Research**

726 7 hours of continuous DAS data (decimated to 10 m channel distance and 100 Hz  
727 sampling rate), and continuous geophones data (3 collocated geophone, A000, R102, R104,  
728 vertical component) have been made available through Zenodo (Zhou et al. 2022), which could  
729 be used to reproduce the seismic noise interferometry and surface wave inversion for S wave  
730 velocity profile.

731

## 732 **References**

733 Ajo-Franklin, J. B., Dou, S., Lindsey, N. J., Monga, I., Tracy, C., Robertson, M., Rodriguez  
734 Tribaldos, V., Ulrich, C., Freifeld, B., Daley, T., & Li, X. (2019). Distributed Acoustic  
735 sensing Using Dark Fiber for Near-surface Characterization and Broadband seismic event  
736 Detection. *Scientific Reports*, 9(1), 1328. <https://doi.org/10.1038/s41598-018-36675-8>

- 737 Alley, R. B. (1987). Firn densification by grain-boundary sliding: a first model. *Le Journal de*  
738 *Physique Colloques*, 48(C1), C1-249-C1-256. <https://doi.org/10.1051/jphyscol:1987135>
- 739 Ashmore, D. W., Hubbard, B., Luckman, A., Kulesa, B., Bevan, S., Booth, A., Munneke, P. K.,  
740 O’Leary, M., Sevestre, H., & Holland, P. R. (2017). Ice and firn heterogeneity within  
741 Larsen C Ice Shelf from borehole optical televIEWing. *Journal of Geophysical Research:*  
742 *Earth Surface*, 122(5), 1139–1153. <https://doi.org/10.1002/2016JF004047>
- 743 Bensen, G. D., Ritzwoller, M. H., Barmin, M. P., Levshin, A. L., Lin, F., Moschetti, M. P.,  
744 Shapiro, N. M., & Yang, Y. (2007). Processing seismic ambient noise data to obtain reliable  
745 broad-band surface wave dispersion measurements. *Geophysical Journal International*,  
746 169(3), 1239–1260. <https://doi.org/10.1111/j.1365-246X.2007.03374.x>
- 747 Booth, A. D., Christoffersen, P., Schoonman, C., Clarke, A., Hubbard, B., Law, R., Doyle, S. H.,  
748 Chudley, T. R., & Chalari, A. (2020). Distributed Acoustic Sensing of Seismic Properties in  
749 a Borehole Drilled on a Fast-Flowing Greenlandic Outlet Glacier. *Geophysical Research*  
750 *Letters*, 47(13). <https://doi.org/10.1029/2020GL088148>
- 751 Brisbourne, A. M., Kendall, M., Kufner, S. K., Hudson, T. S., & Smith, A. M. (2021). Downhole  
752 distributed acoustic seismic profiling at Skytrain Ice Rise, West Antarctica. *Cryosphere*,  
753 15(7), 3443–3458. <https://doi.org/10.5194/tc-15-3443-2021>
- 754 Butcher, A., Hudson, T., Kendall, J., Kufner, S., Brisbourne, A., & Stork, A. (2021). Radon  
755 transform-based detection of microseismicity on DAS networks: A case study from  
756 Antarctica. *EAGE GeoTech 2021 - 1st EAGE Workshop on Induced Seismicity*.  
757 <https://doi.org/10.3997/2214-4609.202131039>
- 758 Butcher, A., Stork, A. L., Verdon, J. P., Kendall, J. M., Plenkers, K., Booth, F., Boneham, M., &  
759 Koe, A. (2021). Evaluating rock mass disturbance within open-pit excavations using

- 760 seismic methods: A case study from the Hinkley Point C nuclear power station. *Journal of*  
761 *Rock Mechanics and Geotechnical Engineering*, 13(3).  
762 <https://doi.org/10.1016/j.jrmge.2020.12.001>
- 763 Case, E., & Kingslake, J. (2022). Phase-sensitive radar as a tool for measuring firn  
764 compaction. *Journal of Glaciology*, 68(267), 139–152. <https://doi.org/10.1017/jog.2021.83>
- 765 Chaput, J., Aster, R., Karplus, M., & Nakata, N. (2022). Ambient high-frequency seismic surface  
766 waves in the firn column of central west Antarctica. *Journal of Glaciology*, 1-14.  
767 <https://doi.org/10.1017/jog.2021.135>
- 768 Cheng, F., Chi, B., Lindsey, N. J., Dawe, T. C., & Ajo-Franklin, J. B. (2021). Utilizing  
769 distributed acoustic sensing and ocean bottom fiber optic cables for submarine structural  
770 characterization. *Scientific Reports*, 11(1), 5613. <https://doi.org/10.1038/s41598-021-84845->  
771 [y](https://doi.org/10.1038/s41598-021-84845-y)
- 772 Cheng, F., Xia, J., Behm, M., Hu, Y., & Pang, J. (2019). Automated data selection in the Tau–p  
773 domain: Application to passive surface wave imaging. *Surveys in Geophysics*, 40(5), 1211-  
774 1228. <https://doi.org/10.1007/s10712-019-09530-2>
- 775 Cheng, F., Xia, J., Luo, Y., Xu, Z., Wang, L., Shen, C., Liu, R., Pan, Y., Mi, B., & Hu, Y.  
776 (2016). Multichannel analysis of passive surface waves based on crosscorrelations.  
777 *GEOPHYSICS*, 81(5), EN57–EN66. <https://doi.org/10.1190/geo2015-0505.1>
- 778 Cheng, F., Xia, J., Xu, Y., Xu, Z., & Pan, Y. (2015). A new passive seismic method based on  
779 seismic interferometry and multichannel analysis of surface waves. *Journal of Applied*  
780 *Geophysics*, 117, 126–135. <https://doi.org/10.1016/j.jappgeo.2015.04.005>
- 781 Correa, J., Freifeld, B. M., Revzner, R., Wood, T., Tertyshnikov, K., & Bona, A. (2018).  
782 Continuous DAS VSP monitoring using surface orbital vibrators: Field trials for optimal

- 783 configuration at the CO2CRC Otway Project. *80th EAGE Conference and Exhibition 2018*  
784 *Workshop Programme*, cp--00040. <https://doi.org/10.3997/2214-4609.201801917>
- 785 Craig, H., Horibe, Y., & Sowers, T. (1988). Gravitational Separation of Gases and Isotopes in  
786 Polar Ice Caps. *Science*, *242*(4886), 1675–1678.  
787 <https://doi.org/10.1126/science.242.4886.1675>
- 788 Cuffey, K. M., & Paterson, W. S. B. (2010). Physics of Glaciers, Fourth Edition. In *The Physics*  
789 *of Glaciers*.
- 790 Diebold, J. B., & Stoffa, P. L. (1981). The travelttime equation, tau-p mapping, and inversion of  
791 common midpoint data. *Geophysics*, *46*(3). <https://doi.org/10.1190/1.1441196>
- 792 Dou, S., Lindsey, N., Wagner, A. M., Daley, T. M., Freifeld, B., Robertson, M., Peterson, J.,  
793 Ulrich, C., Martin, E. R., & Ajo-Franklin, J. B. (2017). Distributed Acoustic Sensing for  
794 Seismic Monitoring of The Near Surface: A Traffic-Noise Interferometry Case Study.  
795 *Scientific Reports*, *7*(1), 11620. <https://doi.org/10.1038/s41598-017-11986-4>
- 796 European Centre for Medium-Range Weather Forecasts (2017). ERA5 Reanalysis,  
797 <https://doi.org/10.5065/D6X34W69>, Research Data Archive at the National Center for  
798 Atmospheric Research, Computational and Information Systems Laboratory, Boulder, Colo.  
799 (Updated monthly.) Accessed 07 Jun 2022.
- 800 Harland, S. R., Kendall, J.-M. ., Stuart, G. W., Lloyd, G. E., Baird, A. F., Smith, A. M.,  
801 Pritchard, H. D., & Brisbourne, A. M. (2013). Deformation in Rutford Ice Stream, West  
802 Antarctica: measuring shear-wave anisotropy from icequakes. *Annals of Glaciology*,  
803 *54*(64), 105–114. <https://doi.org/10.3189/2013AoG64A033>

- 804 He, X., Xie, S., Liu, F., Cao, S., Gu, L., Zheng, X., & Zhang, M. (2017). Multi-event waveform-  
805 retrieved distributed optical fiber acoustic sensor using dual-pulse heterodyne phase-  
806 sensitive OTDR. *Optics Letters*, 42(3), 442. <https://doi.org/10.1364/OL.42.000442>
- 807 Herrmann, R. B. (2013). Computer programs in seismology: An evolving tool for instruction and  
808 research. *Seismological Research Letters*, 84(6). <https://doi.org/10.1785/0220110096>
- 809 Herron, M. M., & Langway, C. C. (1980). Firn densification: an empirical model. *Journal of*  
810 *Glaciology*, 25(93). <https://doi.org/10.1017/S0022143000015239>
- 811 Hollmann, H., Treverrow, A., Peters, L. E., Reading, A. M., & Kulesa, B. (2021). Seismic  
812 observations of a complex firn structure across the Amery Ice Shelf, East Antarctica.  
813 *Journal of Glaciology*, 67(265), 777–787. <https://doi.org/10.1017/jog.2021.21>
- 814 Hudson, T. S., Baird, A. F., Kendall, J. M., Kufner, S. K., Brisbourne, A. M., Smith, A. M.,  
815 Butcher, A., Chalari, A., & Clarke, A. (2021). Distributed Acoustic Sensing (DAS) for  
816 Natural Microseismicity Studies: A Case Study From Antarctica. *Journal of Geophysical*  
817 *Research: Solid Earth*, 126(7). <https://doi.org/10.1029/2020JB021493>
- 818 Ide, S., Araki, E., & Matsumoto, H. (2021). Very broadband strain-rate measurements along a  
819 submarine fiber-optic cable off Cape Muroto, Nankai subduction zone, Japan. *Earth,*  
820 *Planets and Space*, 73(1), 63. <https://doi.org/10.1186/s40623-021-01385-5>
- 821 Jordan, T. M., Martín, C., Brisbourne, A. M., Schroeder, D. M., & Smith, A. M. (2022). Radar  
822 Characterization of Ice Crystal Orientation Fabric and Anisotropic Viscosity Within an  
823 Antarctic Ice Stream. *Journal of Geophysical Research: Earth Surface*, 127(6).  
824 <https://doi.org/10.1029/2022jf006673>

- 825 Jordan, T. M., Schroeder, D. M., Elsworth, C. W., & Siegfried, M. R. (2020). Estimation of ice  
826 fabric within Whillans Ice Stream using polarimetric phase-sensitive radar sounding. *Annals  
827 of Glaciology*, *61*(81), 74–83. <https://doi.org/10.1017/aog.2020.6>
- 828 King, E. C., & Jarvis, E. P. (2007). Use of Shear Waves to Measure Poisson's Ratio in Polar  
829 Firn. *Journal of Environmental and Engineering Geophysics*, *12*(1), 15–21.  
830 <https://doi.org/10.2113/JEEG12.1.15>
- 831 Kirchner, J. F., & Bentley, C. R. (1979). Seismic Short-Refraction Studies on the Ross Ice Shelf,  
832 Antarctica. *Journal of Glaciology*, *24*(90), 313–319.  
833 <https://doi.org/10.3189/S0022143000014830>
- 834 Kirchner, J. F., & Bentley, C. R. (1990). *RIGGS III: Seismic Short-Refraction Studies Using an  
835 Analytical Curve-Fitting Technique* (pp. 109–126). <https://doi.org/10.1029/AR042p0109>
- 836 Krischer, L., Megies, T., Barsch, R., Beyreuther, M., Lecocq, T., Caudron, C., & Wassermann, J.  
837 (2015). ObsPy: a bridge for seismology into the scientific Python ecosystem.  
838 *Computational Science & Discovery*, *8*(1), 014003. [https://doi.org/10.1088/1749-  
839 4699/8/1/014003](https://doi.org/10.1088/1749-4699/8/1/014003)
- 840 Kufner, S., Brisbourne, A. M., Smith, A. M., Hudson, T. S., Murray, T., Schlegel, R., Kendall, J.  
841 M., Anandakrishnan, S., & Lee, I. (2021). Not all Icequakes are Created Equal: Basal  
842 Icequakes Suggest Diverse Bed Deformation Mechanisms at Rutford Ice Stream, West  
843 Antarctica. *Journal of Geophysical Research: Earth Surface*, *126*(3).  
844 <https://doi.org/10.1029/2020JF006001>
- 845 Lellouch, A., Yuan, S., Spica, Z., Biondi, B., & Ellsworth, W. L. (2019). Seismic Velocity  
846 Estimation Using Passive Downhole Distributed Acoustic Sensing Records: Examples

- 847 From the San Andreas Fault Observatory at Depth. *Journal of Geophysical Research: Solid*  
848 *Earth*, 124(7), 6931–6948. <https://doi.org/10.1029/2019JB017533>
- 849 Lindner, F., Laske, G., Walter, F., & Doran, A. K. (2019). Crevasse-induced Rayleigh-wave  
850 azimuthal anisotropy on Glacier de la Plaine Morte, Switzerland. *Annals of Glaciology*,  
851 60(79), 96–111. <https://doi.org/10.1017/aog.2018.25>
- 852 Lindsey, N. J., Rademacher, H., & Ajo-Franklin, J. B. (2020). On the Broadband Instrument  
853 Response of Fiber-Optic DAS Arrays. *Journal of Geophysical Research: Solid Earth*,  
854 125(2), 1–16. <https://doi.org/10.1029/2019JB018145>
- 855 Lior, I., Mercerat, E. D., Rivet, D., Sladen, A., & Ampuero, J.-P. (2021). *Imaging an Underwater*  
856 *Basin and its Resonance Modes using Optical Fiber Distributed Acoustic Sensing*.  
857 <https://doi.org/https://doi.org/10.31223/X5XK8P>
- 858 Lior, I., Sladen, A., Rivet, D., Ampuero, J., Hello, Y., Becerril, C., Martins, H. F., Lamare, P.,  
859 Jestin, C., Tsagkli, S., & Markou, C. (2021). On the Detection Capabilities of Underwater  
860 Distributed Acoustic Sensing. *Journal of Geophysical Research: Solid Earth*, 126(3), 1–20.  
861 <https://doi.org/10.1029/2020JB020925>
- 862 Luu, K. (2021). *disba: Numba-accelerated computation of surface wave dispersion*.  
863 <https://doi.org/https://doi.org/10.5281/zenodo.3987395>
- 864 Mateeva, A., Lopez, J., Chalenski, D., Tatanova, M., Zwartjes, P., Yang, Z., Bakku, S., Vos, K.  
865 de, & Potters, H. (2017). 4D das VSP as a tool for frequent seismic monitoring in deep  
866 water. *Leading Edge*, 36(12), 995–1000. <https://doi.org/10.1190/tle36120995.1>
- 867 Morris, E. M., Mulvaney, R., Arthern, R. J., Davies, D., Gurney, R. J., Lambert, P., De Rydt, J.,  
868 Smith, A. M., Tuckwell, R. J., & Winstrup, M. (2017). Snow Densification and Recent  
869 Accumulation Along the iSTAR Traverse, Pine Island Glacier, Antarctica. *Journal of*

- 870 *Geophysical Research: Earth Surface*, 122(12), 2284–2301.  
871 <https://doi.org/10.1002/2017jf004357>
- 872 Murray, T., Smith, A. M., King, M. A., & Weedon, G. P. (2007). Ice flow modulated by tides at  
873 up to annual periods at Rutford Ice Stream, West Antarctica. *Geophysical Research Letters*,  
874 34(18), L18503. <https://doi.org/10.1029/2007GL031207>
- 875 Olivier, G., Brenguier, F., Campillo, M., Lynch, R., & Roux, P. (2015). Body-wave  
876 reconstruction from ambient seismic noise correlations in an underground mine.  
877 *GEOPHYSICS*, 80(3). <https://doi.org/10.1190/geo2014-0299.1>
- 878 Park, C. B., Miller, R. D., & Xia, J. (1999). Multichannel analysis of surface waves.  
879 *GEOPHYSICS*, 64(3), 800–808. <https://doi.org/10.1190/1.1444590>
- 880 Park, C., Miller, R., Laflen, D., Bennett, B., Ivanov, J., Neb, C., & Huggins, R. (2004). Imaging  
881 dispersion curves of passive surface waves. 2004 SEG Annual Meeting.
- 882 Peters, L. E., Anandakrishnan, S., Alley, R. B., Winberry, J. P., Voigt, D. E., Smith, A. M., &  
883 Morse, D. L. (2006). Subglacial sediments as a control on the onset and location of two  
884 Siple Coast ice streams, West Antarctica. *Journal of Geophysical Research*, 111(B1).  
885 <https://doi.org/10.1029/2005jb003766>
- 886 Porritt, R., Abbott, R., & Poppeliers, C. (2022). Quantitative assessment of Distributed Acoustic  
887 Sensing at the Source Physics Experiment, Phase II. <https://doi.org/10.2172/1855336>
- 888 Ravasi, M., & Vasconcelos, I. (2020). PyLops—A linear-operator Python library for scalable  
889 algebra and optimization. *SoftwareX*, 11, 100361.  
890 <https://doi.org/10.1016/j.softx.2019.100361>
- 891 Riverman, K. L., Alley, R. B., Anandakrishnan, S., Christianson, K., Holschuh, N. D., Medley,  
892 B., Muto, A., & Peters, L. E. (2019). Enhanced Firn Densification in High-Accumulation

- 893 Shear Margins of the NE Greenland Ice Stream. *Journal of Geophysical Research: Earth*  
894 *Surface*, 124(2), 365–382. <https://doi.org/10.1029/2017JF004604>
- 895 Rodríguez Tribaldos, V., & Ajo-Franklin, J. B. (2021). Aquifer Monitoring Using Ambient  
896 Seismic Noise Recorded With Distributed Acoustic Sensing (DAS) Deployed on Dark  
897 Fiber. *Journal of Geophysical Research: Solid Earth*, 126(4), 1–20.  
898 <https://doi.org/10.1029/2020jb021004>
- 899 Rodríguez Tribaldos, V., Ajo-Franklin, J., Dou, S., Lindsey, N., Ulrich, C., Robertson, M.,  
900 Freifeld, B., Daley, T., Monga, I., & Tracy, C. (2019). *Surface Wave Imaging using*  
901 *Distributed Acoustic Sensing Deployed on Dark Fiber: Moving Beyond High Frequency*  
902 *Noise*. <https://doi.org/10.31223/OSF.IO/JB2NA>
- 903 Rücker, C., Günther, T., & Wagner, F. M. (2017). pyGIMLi: An open-source library for  
904 modelling and inversion in geophysics. *Computers & Geosciences*, 109, 106–123.  
905 <https://doi.org/10.1016/j.cageo.2017.07.011>
- 906 Schimmel, M., & Paulssen, H. (1997). Noise reduction and detection of weak, coherent signals  
907 through phase-weighted stacks. *Geophysical Journal International*, 130(2), 497–505.  
908 <https://doi.org/10.1111/j.1365-246X.1997.tb05664.x>
- 909 Schimmel, M., Stutzmann, E., & Gallart, J. (2011). Using instantaneous phase coherence for  
910 signal extraction from ambient noise data at a local to a global scale. *Geophysical Journal*  
911 *International*, 184(1), 494–506. <https://doi.org/10.1111/j.1365-246X.2010.04861.x>
- 912 Schlegel, R., Diez, A., Löwe, H., Mayer, C., Lambrecht, A., Freitag, J., Miller, H., Hofstede, C.,  
913 & Eisen, O. (2019). Comparison of elastic moduli from seismic diving-wave and ice-core  
914 microstructure analysis in Antarctic polar firn. *Annals of Glaciology*, 60(79), 220–230.  
915 <https://doi.org/10.1017/aog.2019.10>

- 916 Sergeant, A., Chmiel, M., Lindner, F., Walter, F., Roux, P., Chaput, J., Gimbert, F., & Mordret,  
917 A. (2020). On the Green's function emergence from interferometry of seismic wave fields  
918 generated in high-melt glaciers: implications for passive imaging and monitoring. *The*  
919 *Cryosphere*, *14*(3), 1139–1171. <https://doi.org/10.5194/tc-14-1139-2020>
- 920 Shapiro, N. M., & Campillo, M. (2004). Emergence of broadband Rayleigh waves from  
921 correlations of the ambient seismic noise. *Geophysical Research Letters*, *31*(7), 8–11.  
922 <https://doi.org/10.1029/2004GL019491>
- 923 Shapiro, N. M., Campillo, M., Stehly, L., & Ritzwoller, M. H. (2005). High-resolution surface-  
924 wave tomography from ambient seismic noise. *Science*, *307*(5715), 1615–1618.
- 925 Shepherd, A., Ivins, E. R., Geruo, A., Barletta, V. R., Bentley, M. J., Bettadpur, S., Briggs, K.  
926 H., Bromwich, D. H., Forsberg, R., Galin, N., Horwath, M., Jacobs, S., Joughin, I., King,  
927 M. A., Lenaerts, J. T. M., Li, J., Ligtenberg, S. R. M., Luckman, A., Luthcke, S. B., ...  
928 Zwally, H. J. (2012). A reconciled estimate of ice-sheet mass balance. *Science*, *338*(6111).  
929 <https://doi.org/10.1126/science.1228102>
- 930 Slichter, L. B. (1932). The Theory of the Interpretation of Seismic Travel-Time Curves in  
931 Horizontal Structures. *Physics*, *3*(6), 273–295. <https://doi.org/10.1063/1.1745133>
- 932 Smith, A. M. (1997). Variations in basal conditions on Rutford Ice Stream, West Antarctica.  
933 *Journal of Glaciology*, *43*(144), 245–255. <https://doi.org/10.3189/S0022143000003191>
- 934 Smith, A. M., Anker, P. G. D., Nicholls, K. W., Makinson, K., Murray, T., Rios-Costas, S.,  
935 Brisbourne, A. M., Hodgson, D. A., Schlegel, R., & Anandakrishnan, S. (2021). Ice stream  
936 subglacial access for ice-sheet history and fast ice flow: the BEAMISH Project on Rutford  
937 Ice Stream, West Antarctica and initial results on basal conditions. *Annals of Glaciology*,  
938 *62*(85–86), 203–211. <https://doi.org/10.1017/aog.2020.82>

- 939 Smith, E. C., Baird, A. F., Kendall, J. M., Martín, C., White, R. S., Brisbourne, A. M., & Smith,  
940 A. M. (2017). Ice fabric in an Antarctic ice stream interpreted from seismic anisotropy.  
941 *Geophysical Research Letters*, *44*(8), 3710–3718. <https://doi.org/10.1002/2016GL072093>
- 942 Smith, E. C., Smith, A. M., White, R. S., Brisbourne, A. M., & Pritchard, H. D. (2015). Mapping  
943 the ice-bed interface characteristics of Rutford Ice Stream, West Antarctica, using  
944 microseismicity. *Journal of Geophysical Research: Earth Surface*, *120*(9), 1881–1894.  
945 <https://doi.org/10.1002/2015JF003587>
- 946 Snieder, R., & Larose, E. (2013). Extracting Earth’s Elastic Wave Response from Noise  
947 Measurements. *Annual Review of Earth and Planetary Sciences*, *41*(1), 183–206.  
948 <https://doi.org/10.1146/annurev-earth-050212-123936>
- 949 Spica, Z. J., Nishida, K., Akuhara, T., Pétrélis, F., Shinohara, M., & Yamada, T. (2020). Marine  
950 Sediment Characterized by Ocean-Bottom Fiber-Optic Seismology. *Geophysical Research*  
951 *Letters*, *47*(16), e2020GL088360. <https://doi.org/10.1029/2020GL088360>
- 952 Spica, Z. J., Perton, M., Martin, E. R., Beroza, G. C., & Biondi, B. (2020). Urban Seismic Site  
953 Characterization by Fiber-Optic Seismology. *Journal of Geophysical Research: Solid*  
954 *Earth*, *125*(3), 1–14. <https://doi.org/10.1029/2019JB018656>
- 955 van den Broeke, M. (2005). Strong surface melting preceded collapse of Antarctic Peninsula ice  
956 shelf. *Geophysical Research Letters*, *32*(12), 1–4. <https://doi.org/10.1029/2005GL023247>
- 957 van den Broeke, M. (2008). Depth and Density of the Antarctic Firn Layer. *Arctic, Antarctic,*  
958 *and Alpine Research*, *40*(2), 432–438. [https://doi.org/10.1657/1523-0430\(07-021\)](https://doi.org/10.1657/1523-0430(07-021))
- 959 van den Ende, M. P. A., & Ampuero, J. P. (2021). Evaluating seismic beamforming capabilities  
960 of distributed acoustic sensing arrays. *Solid Earth*, *12*(4), 915–934.  
961 <https://doi.org/10.5194/se-12-915-2021>

- 962 Vidal, C. A., Draganov, D., van der Neut, J., Drijkoningen, G., & Wapenaar, K. (2014).  
963 Retrieval of reflections from ambient noise using illumination diagnosis. *Geophysical*  
964 *Journal International*, 198(3), 1572–1584. <https://doi.org/10.1093/gji/ggu164>
- 965 Walter, F., Gräff, D., Lindner, F., Paitz, P., Köpfl, M., Chmiel, M., & Fichtner, A. (2020).  
966 Distributed acoustic sensing of microseismic sources and wave propagation in glaciated  
967 terrain. *Nature Communications*, 11(1), 2436. <https://doi.org/10.1038/s41467-020-15824-6>
- 968 Walter, F., Roux, P., Roeoesli, C., Lecointre, A., Kilb, D., & Roux, P. F. (2015). Using glacier  
969 seismicity for phase velocity measurements and Green's function retrieval. *Geophysical*  
970 *Journal International*, 201(3). <https://doi.org/10.1093/gji/ggv069>
- 971 Williams, E. F., Fernández-Ruiz, M. R., Magalhaes, R., Vanthillo, R., Zhan, Z., González-  
972 Herráez, M., & Martins, H. F. (2019). Distributed sensing of microseisms and teleseisms  
973 with submarine dark fibers. *Nature Communications*, 10(1), 1–11.  
974 <https://doi.org/10.1038/s41467-019-13262-7>
- 975 Xia, J., Xu, Y., & Miller, R. D. (2007). Generating an Image of Dispersive Energy by Frequency  
976 Decomposition and Slant Stacking. *Pure and Applied Geophysics*, 164(5), 941–956.  
977 <https://doi.org/10.1007/s00024-007-0204-9>
- 978 Xia, J., Miller, R. D., & Park, C. B. (1999). Estimation of near-surface shear-wave velocity by  
979 inversion of Rayleigh waves. *GEOPHYSICS*, 64(3), 691–700.  
980 <https://doi.org/10.1190/1.1444578>
- 981 Yu, C., Zhan, Z., Lindsey, N. J., Ajo-Franklin, J. B., & Robertson, M. (2019). The Potential of  
982 DAS in Teleseismic Studies: Insights From the Goldstone Experiment. *Geophysical*  
983 *Research Letters*, 46(3), 1320–1328. <https://doi.org/10.1029/2018GL081195>

- 984 Yudistira, T., Paulssen, H., & Trampert, J. (2017). The crustal structure beneath The Netherlands  
985 derived from ambient seismic noise. In *Tectonophysics* (Vol. 721, Issue 77).  
986 <https://doi.org/10.1016/j.tecto.2017.09.025>
- 987 Zhang, X., Paulssen, H., Lebedev, S., & Meier, T. (2007). Surface wave tomography of the Gulf  
988 of California. *Geophysical Research Letters*, 34(15).  
989 <https://doi.org/10.1029/2007GL030631>
- 990 Zhou, W., Butcher, A., Brisbourne, A., Kufner, S., Kendall, J. M., & Stork, A. (2022). Seismic  
991 noise interferometry and Distributed Acoustic Sensing (DAS): measuring the firm layer S-  
992 velocity structure on Rutford Ice Stream, Antarctica (v.0.0.1) [Data set]. Zenodo.  
993 <https://doi.org/10.5281/zenodo.7064405>
- 994 Zhou, W., & Paulssen, H. (2020). Compaction of the Groningen gas reservoir investigated with  
995 train noise. *Geophysical Journal International*, 223(2), 1327–1337.  
996 <https://doi.org/10.1093/gji/ggaa364>  
997

1

2

*JGR Earth Surface*

3

Supporting Information for

4

**Seismic noise interferometry and Distributed Acoustic Sensing (DAS): measuring the firn layer S-velocity structure on Rutford Ice Stream, Antarctica**

5

6

7

Wen Zhou<sup>1</sup>, Antony Butcher<sup>1</sup>, Alex Brisbourne<sup>2</sup>, Sofia-Katerina Kufner<sup>2</sup>, J-Michael Kendall<sup>3</sup>, Anna Stork<sup>4</sup>

8

9

<sup>1</sup>University of Bristol, BS8 1TH, Bristol, UK

10

<sup>2</sup>British Antarctic Survey, CB3 0ET, Cambridge, UK

11

<sup>3</sup>University of Oxford, OX1 2JD, Oxford, UK

12

<sup>4</sup>Silixa, WD6 3SN, Borehamwood, UK

13

Corresponding author: Wen Zhou (wz18709@bristol.ac.uk)

14

**Contents of this file**

16

Text S1

17

Figures S1 to S6

**Introduction**

20

A comparison of noise interferometry and frequency-wavenumber (f-k) domain stacking is provided in Text S1 and Figure S1. DAS noise from 0.01 to 1 Hz is shown in Figure S2. f-k transform of cross-correlations and an active shot are shown in Figure S3. Variations of dispersions curves in Figure S4. Located shear margin seismic events using the geophone array in Figure S5.

25

26 **Text S1. Locating surface wave events with the geophone array**

27 To get an idea of where the surface wave events originated. We use the  
28 geophone array to locate them very roughly. Firstly, a 1 to 10 Hz bandpass filter is  
29 applied. Secondly, we detect the surface wave events based on signal peak amplitude  
30 from a beamforming analysis. Thirdly, for each detected event, we calculate frequency-  
31 dependent arrival time. Lastly, taking the  $V_s$  model obtained in the main text, theoretical  
32 travel time can be calculated for a given location, thus, we apply an inversion to get the  
33 event location. Events which are located with low residuals are plotted in Figure S6.

34 We admit that this process is very rough, and the uncertainties of the locations  
35 are in the order of a few km, due to the small aperture of the array and also that the  
36 velocity is only validated in the centre of the ice stream, while most events are originated  
37 from the mountain areas (Ellsworth Mountain in the West and Fletcher Promontory in  
38 the East). Additional uncertainty might arise from the topography that is not included in  
39 the velocity model.

40

41

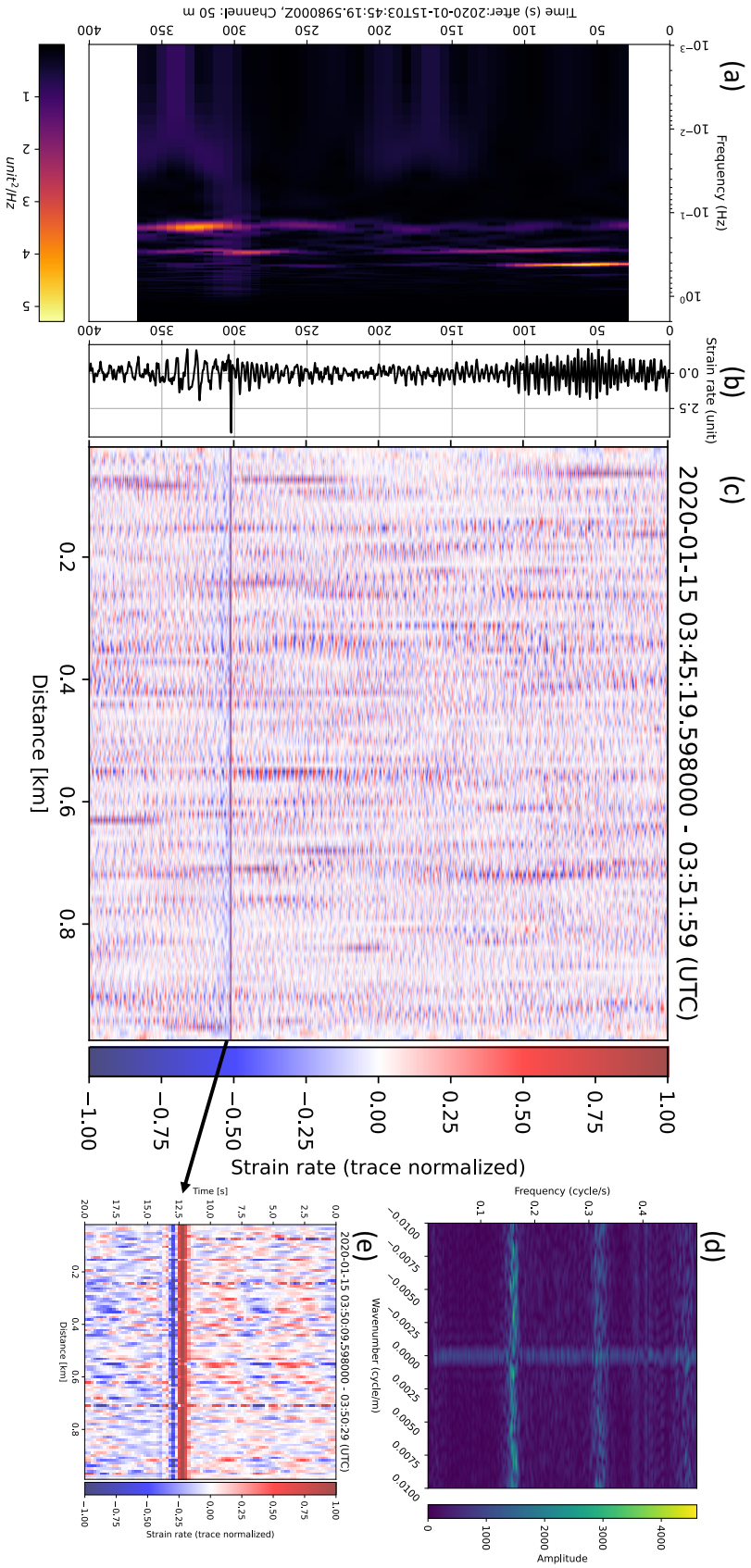
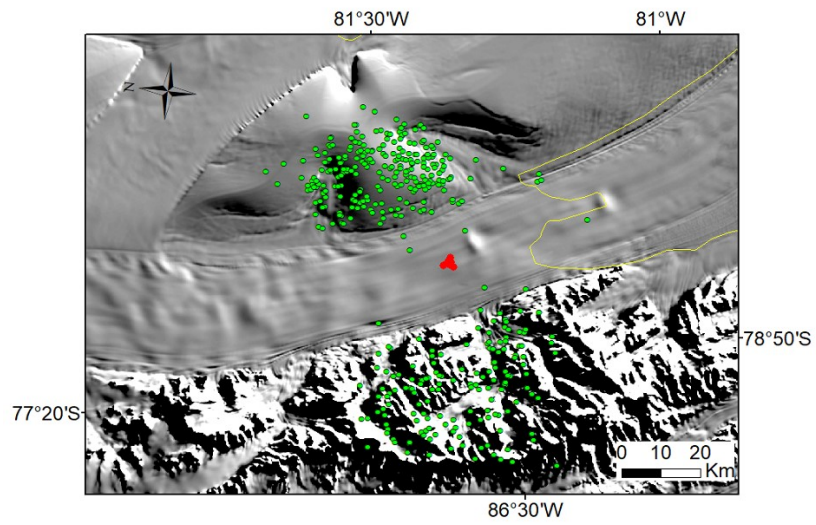


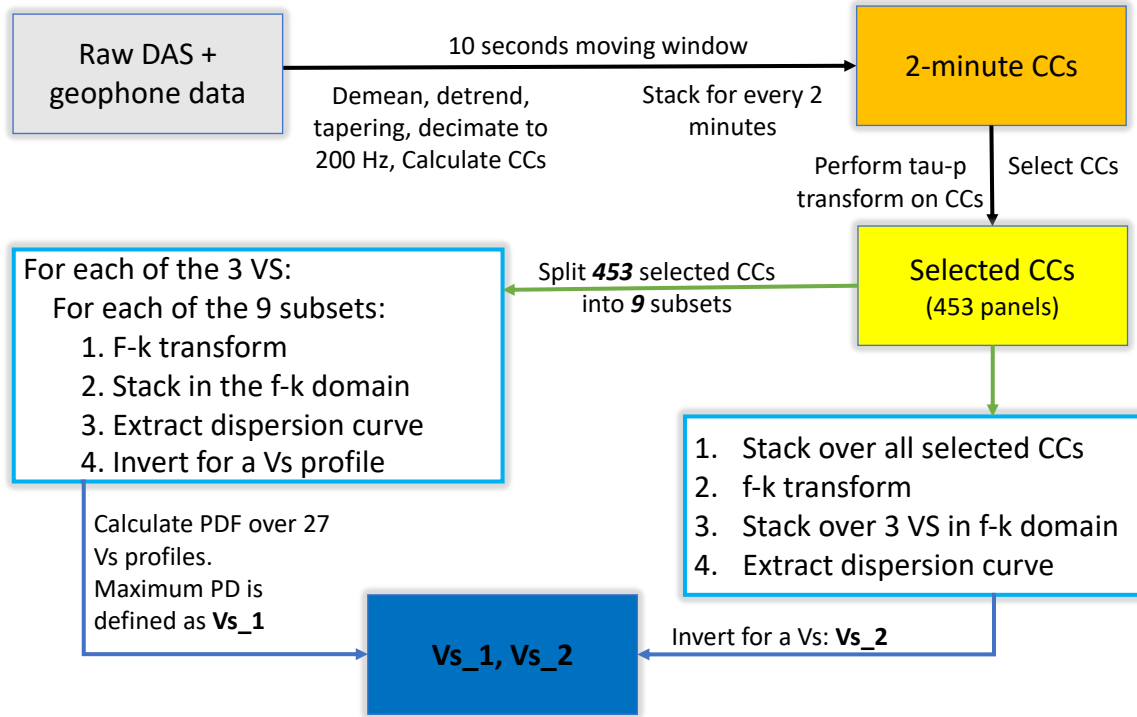
**Figure S1. (c) a 400-second example of noises between 0.01 to 1 Hz. (a) spectrogram of the channel at distance of 50 m. Time series is plotted in panel (b). (d) F-k transform of (c). (e) zoom in of (c) as indicated by the arrow.**

43  
44



45  
46  
47  
48  
49

**Figure S2. Localized surface wave events using the geophone array (red triangles), using travel time difference obtained from waveform cross-correlation.**

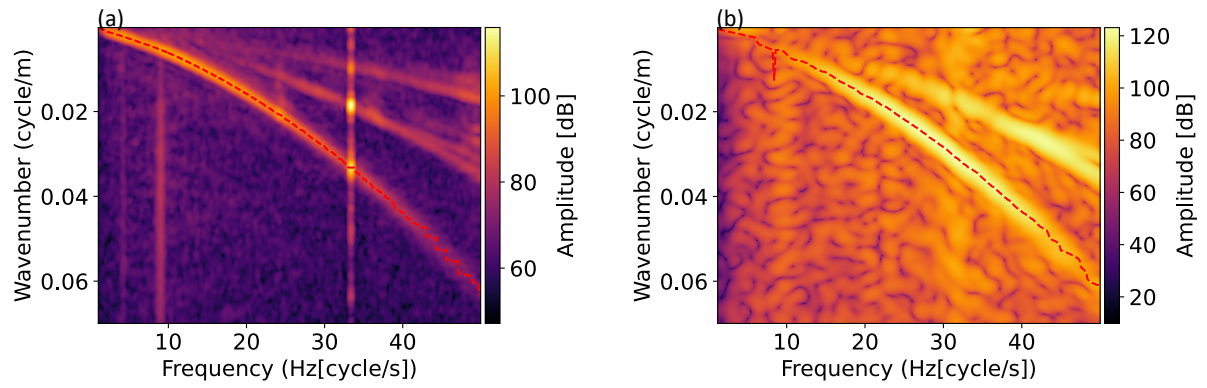


50  
51

Figure S3. Workflow for DAS noise interferometry and surface wave inversion implemented in this study.

52

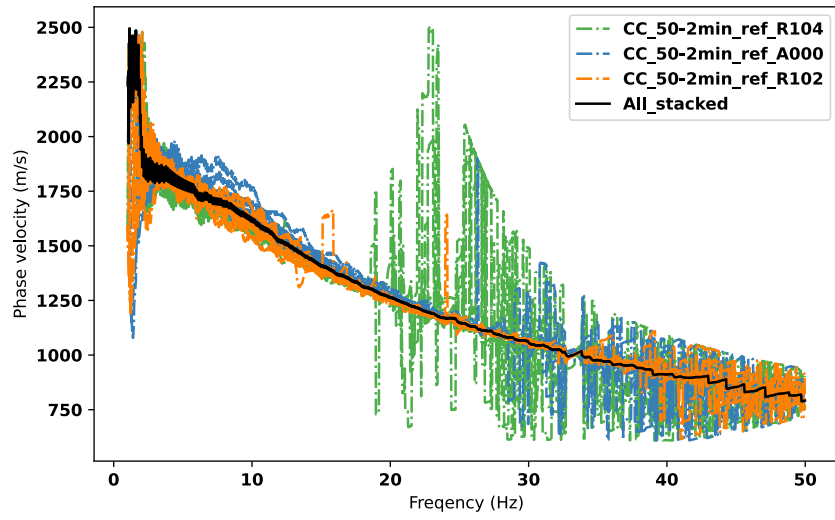
53  
54



55  
56  
57  
58  
59  
60

**Figure S4. Plots of the f-k domain amplitude spectrum. (a) f-k for selective stacked cross-correlations (CCs), with picks of fundamental mode surface wave shown by a dashed line. (b) The same as (a) but for one active shot gather.**

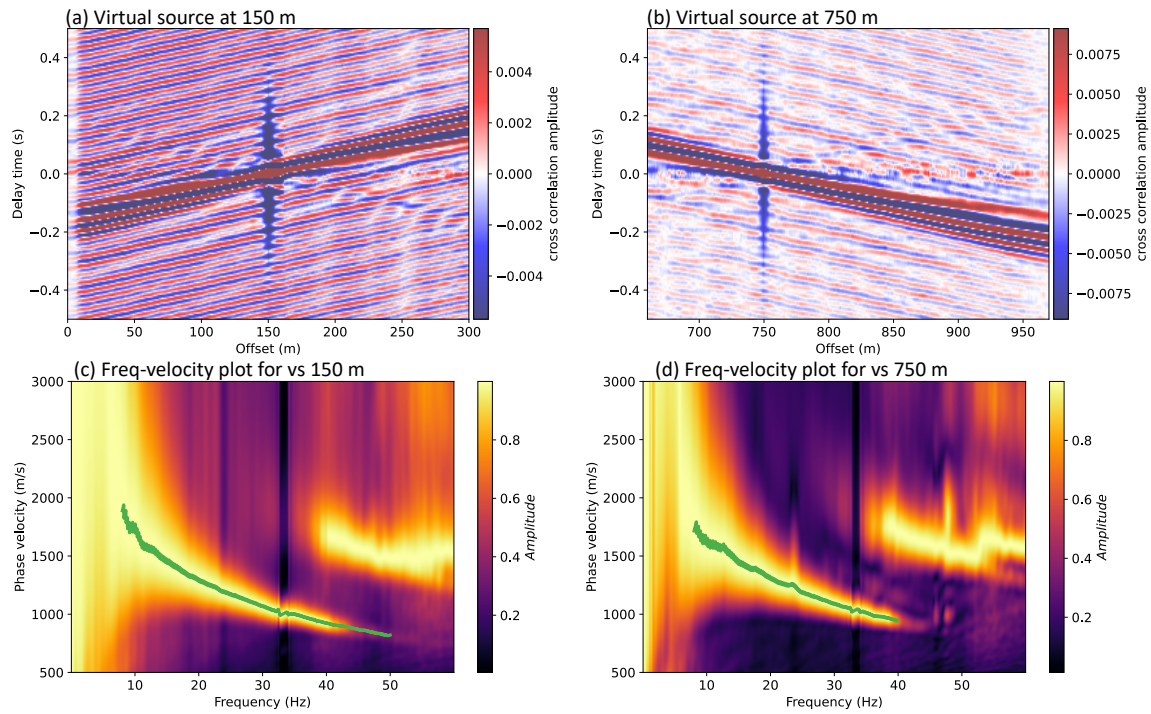
61



62  
63  
64  
65  
66

Figure S5. Variation of dispersions from all 50-2min-CC stacks, compared with the stack over all selected 2-min CCs.

67



68

69

70

71

72

**Figure S6. Stacked CCs and Phase velocity plots from two segments of the triangular array. (a) segment 0 to 330 m, with a virtual source at 150 m. (b) segment 660 to 960 m, with a virtual source at 750 m. (c) Phase velocity plot for virtual source at 150 m and dispersion extraction from 8 to 50 Hz. (d) Phase velocity plot for virtual source at 750 m and dispersion extraction from 8 to 40 Hz.**